Probing Mg Intercalation in Tetragonal Tungsten Bronze Framework $V_4Nb_{18}O_{55}$

Ian D. Johnson,[a]‡ Gene Nolis,[b,c]‡ Kit McColl,[a] Yimin A. Wu,[c,d] Daisy Thornton,[a] Linhua Hu,[b,c] Hyun Deog Yoo,[e] John W. Freeland,[f] Furio Corà,[a] Jeremy K. Cockcroft,[a] Ivan P. Parkin,[a] Robert F. Klie,[d] Jordi Cabana,[b,c*] and Jawwad A. Darr[a*]

[a.] Department of Chemistry, University College London, 20 Gower Street, London, WC1H 0AJ, UK.

[b.] Department of Chemistry, University of Illinois at Chicago, Chicago, IL 60607, USA.

[c.] Joint Center for Energy Storage Research, Argonne National Laboratory, Argonne, IL 60439, USA.

[d.] Department of Physics, University of Illinois at Chicago, Chicago, IL 60607, USA

[e.] Department of Chemistry and Chemical Institute for Functional Materials, Pusan National University, Busan 46241, Republic of Korea.

[f.] X-ray Science Division, Advanced Photon Source, Argonne National Laboratory, Argonne, IL 60439, USA.

‡The contribution of IDJ and GN to this work was equal.

ABSTRACT: While commercial Li-ion batteries offer the highest energy densities of current rechargeable battery technologies, their energy storage limit has almost been achieved. Therefore, there is considerable interest in Mg batteries, which could offer increased energy densities compared to Li-ion batteries if a high-voltage electrode material, such as a transition metal oxide, can be developed. However, there are currently very few oxide materials which have demonstrated reversible and efficient Mg^{2+} insertion and extraction at high voltages; this is thought to be due to poor Mg-ion diffusion kinetics within the oxide structural framework. Herein, the authors provide conclusive evidence of electrochemical insertion of Mg^{2+} into the tetragonal tungsten bronze $V_4Nb_{18}O_{55}$, with a maximum reversible electrochemical capacity of 75 mA h g^{-1}, which corresponds to a magnesiated composition of $Mg_4V_4Nb_{18}O_{55}$. Experimental electrochemical magnesiation/de-magnesiation revealed a large voltage hysteresis with charge/discharge (1.12 V vs Mg/Mg^{2+}); by limiting magnesiation to a composition of $Mg_2V_4Nb_{18}O_{55}$, this hysteresis can be reduced down to only 0.5 V. Hybrid-exchange Density Functional Theory (DFT) calculations suggest that a limited number of Mg sites are accessible via low-energy diffusion pathways, but that larger kinetic barriers need to be overcome to access the entire structure. The reversible Mg-ion intercalation involved concurrent V and Nb redox activity and changes in crystal structure, confirmed by an array of complimentary methods including powder X-ray diffraction, X-ray absorption spectroscopy, and energy-dispersive X-ray spectroscopy. Consequently, It can be concluded that the tetragonal tungsten bronzes show promise as intercalation electrode materials for Mg batteries.

Introduction

With the growing need for high energy-density batteries, the development of new energy storage technologies is paramount. While Li-ion batteries have achieved great commercial success,[1] and are the most energy-dense rechargeable storage technology for portable applications, the technology already heavily optimized, and future increases in energy density are predicted to be incremental.[2] Therefore, there is a need to develop new, low cost, and sustainable battery chemistries for applications such as future electric vehicle and grid storage. Mg metal anodes have a lower propensity to form dendrites (that can cause cell failure) from stripping and plating, which means that it could be used directly as a metallic anode,[3–5] which would offer up to a five-fold increase in anodic volumetric energy density (Mg metal = 3833 mA h cm^{-3}) compared to Li-ion graphite anodes (~800 mA h cm^{-3}), leading to an overall doubling in energy density if a suitably high-energy density electrode material can be found.[6] In comparison to Li^+, the divalent ion Mg^{2+} transfers twice the charge (2 e^- per Mg^{2+} ion) when moving between anode and cathode. This phenomenon decouples the effect of electronic changes from the availability of vacant sites in the crystal structure, creating opportunities to create novel fundamental insights into the limits of intercalation electrochemistry. Furthermore, the Mg battery offers a step-change in sustainability; Mg is three orders of magnitude more abundant than Li in the Earth's crust, and can be harvested from a range of commercial sources, including seawater.[7] Finally, if Mg batteries were developed, it would be possible to repurpose existing Li-ion battery pilot lines for their manufacture without the large expense and technical challenges of a completely new plant design.

Achieving reversible Mg^{2+} insertion within electrode material candidates at desirable cathodic potentials (> 2 V vs. Mg/Mg^{2+}) has proved extremely challenging; whilst the Mg^{2+} ion possesses a similar ionic radius to Li^+ (0.72 vs 0.76 Å respectively),[8] the increased charge of the former, results in stronger bonding interactions with anions in both the host electrode structure and the electrolyte. Consequently, both Mg-ion diffusion in the electrode structure, and Mg-ion

transfer between electrolyte and electrode, are suggested to present much higher kinetic barriers to reversible intercalation compared to Li^+. Therefore, stable materials which reversibly cycle against Mg metal anodes, have largely consisted of heavy metal chalcogenides such as sulfides, where the soft nature of the sulfide anion leads to weaker anion-intercalant interactions. Therefore, more facile Mg intercalation kinetics.[9–11] However, the operating voltages of sulfides vs. Mg/Mg^{2+} are too low to achieve higher energy density than even first-generation Li-ion cells.[12][12,13] Therefore, oxide hosts, which are typically lighter and can allow higher voltages vs. Mg/Mg^{2+}, are of great interest as electrode materials for devices with high energy densities.[14–18] In comparison, there has also been numerous studies of alternative electrode chemistries, including Prussian Blue analogues,[19] selenides,[20] phosphates,[21] silicates,[22] titanates,[23] and borates.[24]

Recent studies on Mg battery anodes have confirmed that a far more comprehensive and holistic approach is required to irrefutably verify reversible Mg intercalation in oxide hosts, i.e. chemical evidence of changing Mg content, spectroscopic evidence (e.g. XAS) of changing redox states in the host material, and evidence of crystal structure changes (from XRD and/or PDF analysis).[17,25] To date, this comprehensive approach has only been conducted on relatively few structures including the λ polymorph of MnO_2, and the α and ζ polymorphs of V_2O_5.[14,26–28] Many other reports have not provided a full, comprehensive proof of Mg-ion intercalation by combining chemical, diffraction, and spectroscopic methods.[29]

The importance of this holistic approach (required to confirm intercalation) is demonstrated in the literature in several instances. For example, α-V_2O_5 has a wide range of reported capacities, which heavily depends on the water content within the structure or electrolyte.[27,30] Unfortunately, the existence of H_2O is precluded in a Mg battery because of its severe incompatibility with the metal anode. Furthermore, Verrelli *et al*. identified that significant proton (H^+) intercalation can take place instead of Mg^{2+} under many conditions, arising from residual water present in the electrolyte, or from H^+ generated from electrolyte decomposition.[31] Furthermore, other oxides (such as α-MoO_3) are prone to competing conversion reactions, and irreversible MgO formation, with cycling.[16]

For the above reasons, there are a dearth of suitable oxide candidates for Mg battery electrodes, and therefore there are significant efforts to find a material with the combination of capacity, voltage, and kinetics required for an energy-dense, energy-efficient Mg battery. The greatest capacity achieved for an oxide electrode (α-V_2O_5) in a very dry electrolyte is 140 mA h g^{-1} (room temperature), and >280 mA h g^{-1} (110 °C),[28,32] but the efficiency of the Mg-ion insertion/removal was poor in both cases, (voltage hysteresis of 0.7 and 0.8 V, respectively). While unconfirmed at present, it was suggested the source of these high kinetic barriers were strong interactions between Mg^{2+} and the host oxide lattice. Therefore, structures with intrinsically high intercalant-diffusion properties could remove the kinetic bottleneck observed within oxide electrodes. Fundamentally, the number of oxides that can intrinsically intercalate Mg^{2+} remains small at present, which hampers our ability to understand design rules for effective intercalation.

Bronze-type frameworks such as $V_4Nb_{18}O_{55}$ are composed of corner-sharing polyhedra along the *c* axis, provide large diffusion planes which can accommodate intercalated ions. The T-Nb_2O_5 phase, or the related bronze-type and Wadsley-Roth crystallographic shear phases $V_4Nb_{18}O_{55}$, $Nb_{18}W_{16}O_{93}$, and $Nb_{16}W_5O_{55}$, have been shown to have very low barriers to Li^+ diffusion in the bulk phase.[33,34] For example, the activation energy barrier for Li^+ self-diffusion in T-Nb_2O_5 was found to be in the range 58 to 91 meV (from NMR studies) in comparison a typical Li-ion intercalation anode (760 meV for spinel-structured $Li_4Ti_5O_{12}$).[35,36]

The advantages of bronze-type phases can be understood using a comparison with the related structure of ReO_3, in which octahedral Re^{6+} ions form a corner sharing MO_6 octahedral framework (i.e. a perovskite with vacant A sites). ReO_3 can accommodate Li^+ in the vacant interstices; however, correlated rotations to the MO_6 octahedra upon Li incorporation act to stabilize the Li ions, distorting the structure, limiting ionic mobility and resulting in capacity fade.[37] In contrast, bronze structures containing M^{5+} ions, such as T-Nb_2O_5 and $V_4Nb_{18}O_{55}$, can resist such framework distortions and offer a more rigid network for reversible metal intercalation.[33,38] The edge-sharing polyhedra present within *ab* planes provide a critical increase in framework rigidity (in comparison with corner-sharing only frameworks). Upon Li^+ or Mg^{2+} incorporation, the polyhedra are effectively locked in place by shared edges and cannot tilt. Therefore, the inserted ions remain in a 'frustrated' coordination, and can diffuse through the structure with low energy barriers.[39,40] Bronze frameworks are therefore candidate materials for high Mg^{2+} mobility electrodes.

Herein, we report the electrochemical characterization of $V_4Nb_{18}O_{55}$ (which possesses a distorted T-Nb_2O_5 structure) in Mg^{2+} electrolytes. The structure was solved in 2010 by Börrnert *et al*,[41] and first reported as a high-power anode material in Li-ion batteries by Qian *et al.* in 2018.[38] $V_4Nb_{18}O_{55}$ shows the intrinsic ability to reversibly intercalate Mg^{2+} with lower hysteresis than known oxide materials (0.5 vs 0.7 V). This was supported by hybrid-exchange DFT investigations, which revealed $V_4Nb_{18}O_{55}$ possessed low-energy Mg diffusion pathways (ca. 0.65 eV activation energy barrier), and suggested design rules for new high Mg-mobility oxide materials based on the tetragonal tungsten bronzes. We confirm that $V_4Nb_{18}O_{55}$ possesses reduced overpotentials and greater energy efficiency than comparable reported oxide materials in dry electrolyte where Mg-ion intercalation is backed-up with a combination of XRD, XAS and elemental evidence (Table 1), albiet with low observed capacity.

Table 1. A summary of different Mg battery electrode materials and their energy densities.

Material	Gravimetric Energy Density / W h kg^{-1}	Applied Current	Energy efficiency / %	Cycling Temperature / °C	Reference	Degree of characterization of discharged and charged states
Chevrel-Mo_6S_8	77	C/2 (0.3 mA cm^{-2})	~95	60	11	Fully characterized
Spinel-Ti_2S_4	228	C/20 (10 mA g^{-1})	~95	60	13	Fully characterized
CuS nanoparticles	250	C/3 (100 mA g^{-1})	~60	50	12	No elemental or structural characterization
$TiSe_2$	108	C/22 (5 mA g^{-1})	~65	25	20	No redox characterization
orthorhombic-V_2O_5	660	C/20 (15 mA g^{-1})	~65	110	28	Fully characterized
$Mo_{2.48}VO_{9.93}$	~250	C/40 (4 mA g^{-1})	~88	25	29	No elemental or redox characterization
MoO_3	270	C/15 (80 μA cm^{-2})	~70	25	16	No elemental or redox characterization
$FePO_4F$	99	C/20 (8.5 mA g^{-1})	~70	25	21	No elemental or redox characterization
$FeSiO_4$	825	C/50 (6.62 mA g^{-1})	~75	55	22	No elemental or redox characterization
Cr-doped $Li_4Ti_5O_{12}$	~60	C/10 (17.5 mA g^{-1})	~60	25	23	No structural or redox characterization
$Ni(CN)_6{\cdot}nH_2O$	102	C/5 (10 mA g^{-1})	~95	25	19	No elemental/redox characterization, electrolyte contained H_2O
$V_4Nb_{18}O_{55}$ ~~(this work)~~[a]	75	C/3 (15 mA g^{-1})	81	110	This work[a]	?????add
$V_4Nb_{18}O_{55}$ ~~(this work)~~[b]	183	C/3 (15 mA g^{-1})	56	110	This work[b]	?????add

[a] Where the capacity was limited to 30 mA h g^{-1}. [b] where the cell was cycled to the limits of the electrolyte stability window, corresponding to 75 mA h g^{-1}.

Experimental Section

Phase-pure $V_4Nb_{18}O_{55}$ nanoparticles were synthesized *via* a two-step process of Continuous Hydrothermal Flow Synthesis (CHFS) of an amorphous Nb/V oxide solid-solution, followed by a 5 h heat-treatment step in air at 600 °C. The details of the CHFS process are described in detail in previous publications, and a diagram of the process is given in Figure S1a in the Supporting Information (SI).[42,43] Briefly, the CHFS process consisted of three high-pressure diaphragm pumps, which provided three separate pressurized feeds into a Confined Jet Mixer (CJM, Figure S1b) which is where mixing of reagents and initial precipitation occurred. A V^{4+} aqueous precursor was prepared using protocol described in the SI. The V^{4+} precursor was diluted with D.I. water and combined with ammonium niobium oxalate hydrate (hydrated $C_4H_4NNbO_9$, 99.99%, Sigma Aldrich, Dorset, UK) to give a combined precursor solution with 36.4 mM and 163.6 mM V^{4+} and Nb^{5+}, respectively, i.e. a 4:18 V:Nb molar ratio, with a total metal concentration of 0.2 M. This combined precursor solution was pumped (via pump 2, flow rate of 40 mL min^{-1}) to mix with an aqueous flow of room temperature D.I. water (in-flow dilution, delivered via pump 3, flow rate of 40 mL min^{-1}) in a T-piece. The resulting solution was subsequently mixed with a superheated water feed at 450 °C (via pump 1, flow rate of 80 mL min^{-1}) in the CJM. This CJM was designed to eliminate any possible blockages under typical experimental conditions, and to enable rapid, turbulent mixing [Reynolds number (Re) > 6900] of the incoming hot and cold feeds. The mixing temperature in the CJM was *ca*. 335 °C, and the residence time was *ca*. 7.2 s before the nanoparticle slurry was cooled in-flow via a pipe-in-pipe heat exchanger and continuously collected at *ca*. 40 °C from the exit of a backpressure regulator valve [which maintained the pressure of the whole system at 24 MPa (Tescom Model 26-1700, Tescom BPR, Hamilton, UK)]. The

resulting particle slurry was cleaned by dialysis until the conductivity of the supernatant was < 60 μS^{-1}. The concentrated aqueous sludge was then frozen at −40 °C and slowly heated from −40 to 25 °C in a VirTis Genesis 35 XL at *ca*. 13 Pa for 24 h. The resulting amorphous V and Nb oxide was heat-treated at 600 °C for 5 hours (1 °C min^{-1} ramp rate) in a furnace (air atmosphere) to yield the phase-pure $V_4Nb_{18}O_{55}$ product.

The Powder X-Ray Diffraction (PXRD) pattern of the pristine material was collected using a Stoe StadiP diffractometer in transmission mode (coupled θ-2θ geometry), using Mo-Kα radiation (λ = 0.709 Å), with the sample contained in a borosilicate capillary. Three patterns were collected in the 2θ range of 2 to 40°, with a step size of 0.5° in 2θ and a collection time of 100 s per step, and these three patterns were combined into one to generate the final diffraction pattern. The PXRD pattern of the demagnesiated (charged) electrode was collected on Bruker D8 Advance X-ray Diffractometer (Cu-Kα radiation, λ = 1.54 Å) in reflection mode. Synchrotron PXRD measurements (λ = 0.413 Å) were performed on an electrochemically magnesiated $V_4Nb_{18}O_{55}$ sample at 11-BM, Advanced Photon Source, Argonne in a Kapton capillary. Rietveld refinement was performed using RIETICA software.

Transmission Electron Microscopy (TEM) and Energy-Dispersive Spectroscopy (EDS) images of the pristine $V_4Nb_{18}O_{55}$ were collected using a 200 keV JEOL JEM-2100 TEM fitted with an Oxford Instruments X-MaxN 80-T Silicon Drift Detector (SDD, GATAN) and processed with AZtec® software. TEM and EDX on magnesiated and demagnesiated electrodes was performed using JEOL-3010 microscope operated at 300 kV. Samples were prepared for imaging by dispersing them in methanol (with the aid of ultrasonication) and pipetting a drop of the resulting suspension onto carbon-coated Cu TEM grids (Agar Scientific, UK). The solvent was then evaporated, leaving a deposition of particles on the grid which was then inserted into the TEM microscope for analysis.

X-ray absorption spectroscopy (XAS) measurements in transmission mode were taken of the sample at the vanadium K-edge (*ca.* 5465 eV) and Nb K-edge (*ca*. 18986 eV) at the B18 beamline at Diamond Light Source (UK). Nb L_3-, V $L_{2,3}$- and O K-edge XAS was performed at the beamline 4-ID-C, Advanced Photon Source, Argonne National Laboratory, USA. At 4-ID-C, spectroscopy was completed simultaneously in both the Total-Electron-Yield (TEY) and Total-Fluorescence Yield (TFY) mode utilizing photocurrent for the TEY and a silicon drift diode detector for the TFY, in order to make direct surface to bulk comparisons. Data were obtained at a spectral resolution of ~0.2 eV, with a 2 s dwell time. 3 scans were performed on each sample, at each absorption edge, and scans were averaged in order to maximize the signal to noise ratio. The Nb L_3-edge was scanned in the range 2360 to 2440 eV and V $L_{2,3}$- and O K-edges were scanned in the range 500 to 560 eV. The V and O energy scales were normalized using a $SrTiO_3$ standard.

Electrodes were prepared by hand-grinding the active material with conductive carbon SuperP® (MTI Corp., California, USA) and binder in an active material:carbon:binder ratio of 60:20:20 wt%. The binder was polyvinylidene difluoride (Solef® PVDF, Solvay Inc., Illinois, USA) dissolved in N-methylpyrrolidone (NMP) (Sigma-Aldrich, Missouri, USA) as a 6 wt% solution. The electrode slurry was cast on 1/2" stainless steel 316 mesh electrodes (325 x 325 wire cloth, Gerard Daniel Worldwide, Pennsylvania, USA) or 30 µm thick Al foil and allowed to dry overnight in air. These electrodes were dried under an IR lamp, and pressed at 8 tons between two pieces of 8 x 8 cm^2 stainless steel to improve contact between active material and current collector, and further dried at 100 °C overnight under vacuum (model 1407 Shel Lab Economy Vacuum Oven). The electrodes possessed active material loadings in the range 2.2 to 4.1 mg cm^{-2}. For the synchrotron XRD electrode, the magnesiated material was extracted from the cell and sealed in a borosilicate glass capillary.

Dried electrodes were assembled into 2032 coin-type cells in an Ar-filled glovebox (water and oxygen ≤ 0.1 ppm). Electrochemical cells contained an activated carbon cloth as a counter electrode (ACC, ACC-5092-20, American Technical Trading Inc., Pleasantville, New York, USA), a glass fiber separator (grade 691, 28297-289, VWR International, USA) and 0.5 M $Mg[N(SO_2)_2(CF_3)_2)_2$-$(C_9H_{20}N)(N(SO_2)_2(CF_3)_2]$ ionic liquid electrolyte (abbreviated as $MgTFSI_2$-$PY_{14}TFSI$) with low H_2O content (~43 ppm). The electrolyte was made by dissolving $MgTFSI_2$ (M1208c, Solvionic, France) in $PY_{14}TFSI$ (Pyr0408a, Solvionic, France). For these 2-electrode cells, the potential of cathode was calibrated by considering the ACC anode potential, which was originally 2.2 V vs Mg/Mg^{2+} and linearly proportional to the state-of-charge (SoC).[32] The polarization of the ACC electrode was quantified by measuring the voltage change of a symmetric ACC|ACC cell with SoC, using the same electrolyte and cycling temperature used for the ACC|$V_4Nb_{18}O_{55}$ cells. Subtracting the capacitive contributions from the measured potential vs. ACC allowed for the determination of the cathodic voltage vs. carbon and vs. Mg/Mg^{2+} as a function of the SoC.

Electrochemistry was carried out at 110 °C in the potential ranges 1.2 to −1.7 V or 1.2 to −2.5 V vs. ACC as indicated in the text. The charge/discharge rate (15 mA g^{-1} which corresponds to a C/3 C-rate assuming a maximum capacity of 75 mA h g^{-1}) was galvanostatically controlled by a Bio-Logic VMP3 potentiostat. After magnesiation and demagnesiation of the $V_4Nb_{18}O_{55}$ samples, the electrodes were recovered, rinsed in acetonitrile five times, and dried at room temperature under vacuum for 1 minute before characterization.

To investigate the discharged state, an electrode was discharged to −1.7 V vs ACC, yielding a capacity of 68 mA h g^{-1} (on a stainless-steel grid electrode substrate, Figure S3a), which corresponds to a theoretical stoichiometry of $Mg_{3.5}V_4Nb_{18}O_{55}$, with mass loading 4.1 mg cm^{-2}, and will hereafter be labelled as "VNO(Discharged_1)". For the High-Angle Annular Dark-Field Scanning Transmission Electron Microscopy (HAADF-STEM) elemental mapping, an electrode (mass loading 2.89 mg cm^{-2}) was discharged to a capacity of 160 mA h g^{-1} (Figure S3b) and named "VNO(Discharged_2)". For the XRD analysis, an electrode was prepared on Al foil (mass loading 3.8 mg cm^{-2}), as Al is much less attenuating than stainless steel thereby giving a

greater signal to noise ratio , and similarly discharged to −1.7 V vs ACC, yielding a similar capacity to VNO(Discharged_1) of 67 mA h g^{-1} and this sample was labelled "VNO(Discharged_3)" (Figure S3c).

To investigate the reversibility of the Mg insertion/removal process, two charged electrodes were produced; the first charged electrode (mass loading 2.7 mg cm^{-2}) was cycled in conditions mimicking the reversible cycling behavior seen in Figure 4a, i.e. a discharge of 75 mA h g^{-1}, followed by a charge of 75 mA h g^{-1}, and this sample is hereafter named "VNO(Charged_1)" (Figure S3d). The second charged electrode (mass loading 2.2 mg^{-1}) was discharged to a greater capacity (137 mA h g^{-1}) and subsequently overcharged (300 mA h g^{-1}), to further investigate the irreversibility of the Mg insertion reaction, generating an electrode that was labelled as "VNO(Charged_2)" (Figure S3e). First-principles calculations were performed using the periodic Density Functional Theory (DFT) code CRYSTAL17.[44] Electronic exchange and correlation were approximated using the hybrid- exchange functional PBE0, which is known to give accurate estimates of the band structure of metal oxide systems with highly correlated electrons,[45] and is efficiently implemented in the CRYSTAL code. All-electron atom-centered Gaussian basis sets were used for all atoms, available from the CRYSTAL online database (www.crystal.unito.it), indicated by the following labels: Nb (Nb_986-31(631d)G_dallolio_1996), V (V_86-411d31G_harrison_1993), O (O_8-411d1_cora_2005), Li (Li_5-11(1d)G_baranek_2013_$LiNbO_3$). The Coulomb and exchange series were truncated with thresholds of 10^{-7}, 10^{-7}, 10^{-7} and 10^{-14}. Reciprocal space was sampled using a Pack-Monkhorst net,[46] with a shrinking factor of IS = 4 along each periodic direction. The self-consistent field (SCF) procedure was performed up to a convergence threshold of $\Delta E = 10^{-8}$ Hartree per unit cell. Full geometry optimizations (lattice parameters and atomic positions) were performed using the default convergence criteria in CRYSTAL17. Grimme's semiclassical D3 scheme to account for the effects of dispersion was used to give an improved structural description.[47–49]

Results and Discussion

$V_4Nb_{18}O_{55}$ possesses an orthorhombic crystallographic unit cell and belongs to the *Cmmm* space group (no. 65) with lattice parameters a = 17.355 Å, b = 17.698 Å and c = 3.971 Å. The structure of $V_4Nb_{18}O_{55}$ is related to the family of tetragonal tungsten bronzes (M_xWO_3, where M = Na, K, Pb, Sn), in which corner-sharing WO_6 octahedra are linked through their axial O-ions in the c direction, and equatorial O-ions in the ab plane. This results in a WO_3 framework displaying three, four and five-member ring tunnels extending in the c direction, with partial occupancy of the 5-membered rings with the large M cations such as Na^+ (Figure 1a,b). In $V_4Nb_{18}O_{55}$, however, some of the 5-member rings are occupied by 7-coordinated pentagonal bipyramidal Nb^{5+} ions, which are edge-sharing with neighboring octahedral units in the ab plane, forming flower-like topology (Figure 1c). These edge-sharing NbO_7 units provide the structural rigidity to avoid correlated polyhedral rotations or other unfavorable distortions upon ion intercalation, which is missing from the M_xWO_3 framework.

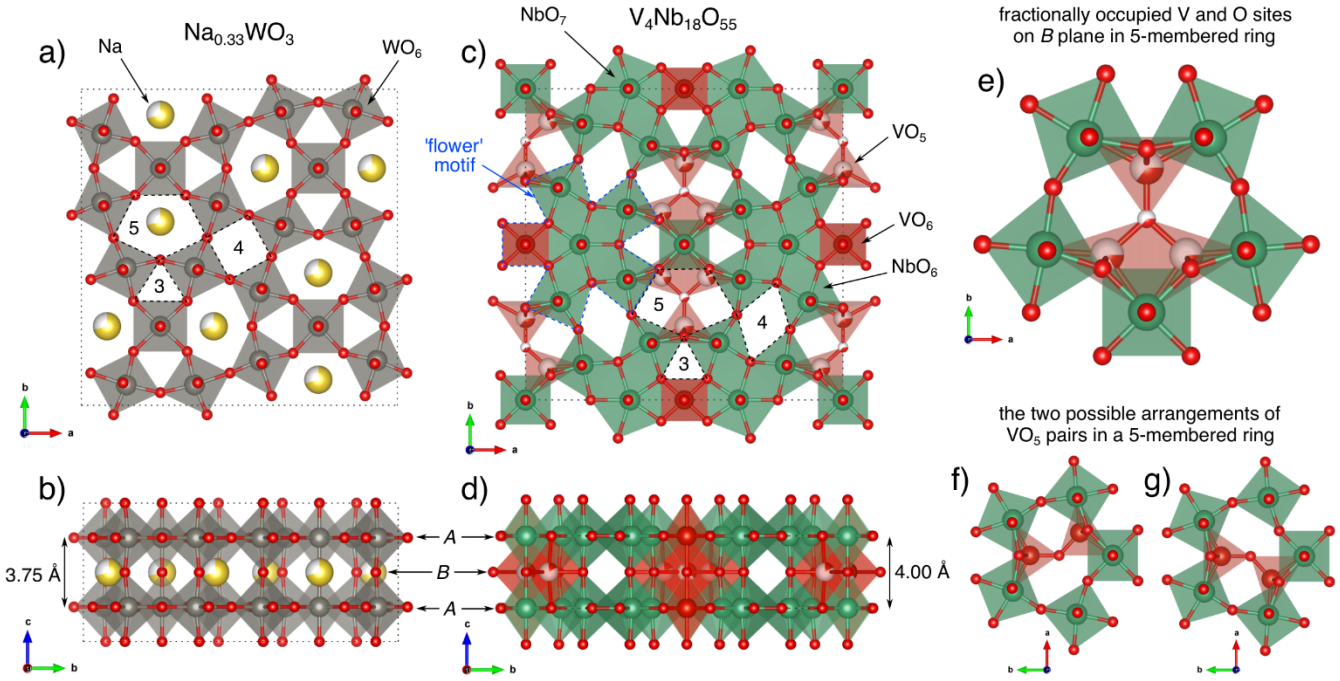

Figure 1. a) A ($\sqrt{2}\times\sqrt{2}\times2$) unit cell of a prototypical tetragonal tungsten bronze $Na_{0.33}WO_3$ viewed along the c direction and b) viewed along the ab plane, highlighting the metal-rich 'A' and oxygen-rich 'B' planes. c) The crystallographic unit cell of $V_4Nb_{18}O_{55}$ viewed along the c direction, and d) viewed along the ab plane. The 3, 4 and 5-membered rings are indicated in both the structures by the black dotted lines. e) 5-memberd rings, fractionally occupied by V and O-ions. f) and g) Possible geometric arrangements of VO_5 pairs in the 5-membered rings.

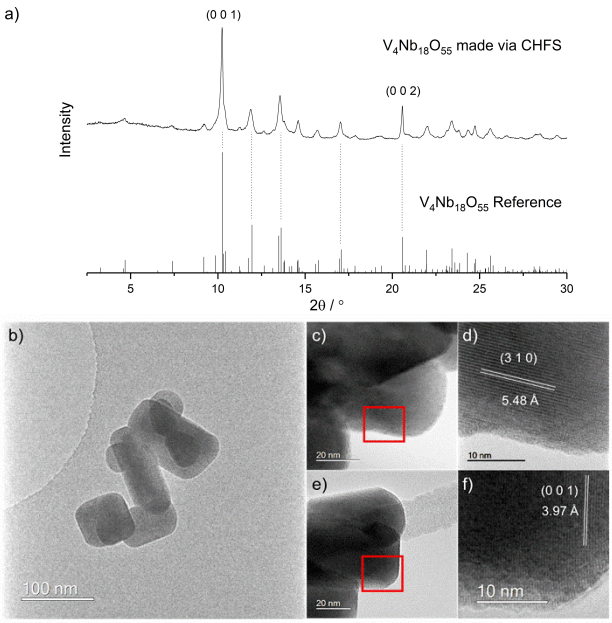

Figure 2. a) The XRD pattern (Mo-Kα radiation, λ = 0.709 Å) of the $V_4Nb_{18}O_{55}$ sample with a $V_4Nb_{18}O_{55}$ reference pattern (ICSD 420781) at the bottom, with the (0 0 1) and (0 0 2) diffraction peaks highlighted (top). Dotted lines have been superimposed on the diagram to highlight peak-matching between the reference pattern and the experimental pattern. TEM images of the $V_4Nb_{18}O_{55}$ sample: b) a representative cluster of $V_4Nb_{18}O_{55}$ nanoparticles, c) a rod identified by TEM analysis, with a selected area for lattice plane analysis shown by a red rectangle, d) lattice plane analysis of the area highlighted in c), e) a separate rod identified by TEM analysis, with a selected area for lattice plane analysis shown by a red rectangle, f) lattice plane analysis of the area highlighted in e).

The octahedra bridging between these NbO_7 units are VO_6, rather than NbO_6. A distinctive feature of W and Nb bronze-type frameworks are layered metal-rich '*A*' and oxygen-rich '*B*' planes when the structure is viewed along *ab* planar directions (Figures 1b,d). The *c*-parameter length of ~4 Å in $V_4Nb_{18}O_{55}$ is similar to that of T-Nb_2O_5, and is typical of structures with axial corner sharing NbO_6 octahedra in this direction. A key structural feature of $V_4Nb_{18}O_{55}$ is the fractional occupation of some of remaining 'empty' (i.e. not occupied by Nb^{5+} ions) 5-membered rings by pairs of trigonal-bipyramidal VO_5 units, which share a bridging O-ion (Figure 1e). These VO_5 pairs occupy ~35% of the 'empty' 5-membered rings, are disordered throughout the lattice, and reside on the '*B*' plane, in contrast to the 'structural' Nb and V ions on the '*A*' plane. There are two possible arrangements of the VO_5 pairs, indicated in Figures 1f and 1g. Note that the VO_5 pairs are always arranged sharing an O-ion across a corner, and never share an edge. $V_4Nb_{18}O_{55}$ was successfully synthesized in a two-step synthesis process, as described in the Methods section. PXRD data analysis revealed that the material possessed the pure $V_4Nb_{18}O_{55}$ structure (*Cmmm* space group), with peaks that had an excellent match with the reference pattern (ICSD collect code 420781, Figure 2a). LeBail refinement of the diffraction pattern revealed lattice parameters of a = 17.3658(12) Å, b = 17.6500(14) Å, c = 3.97886(6) Å, V = 1219.55(13) Å, which are in concordance with the values reported by Börrnert *et al.* (Figure S2a).[41]

The diffraction peaks with *hkl* indices (0 0 1) and (0 0 2) displayed enhanced intensities with respect to the calculated intensities. This was most visible in the LeBail fit of this material in Figure S2a, where the fit included a (0 0 1) texture term. This suggested that the material formed rod-type particles (with the long axis aligned with the *c* direction). This was confirmed by TEM analysis, which revealed that the primary particles possessed a rod-like morphology (Figure 2b). The long-axis of these particles was shown to be parallel to the *c*-axis, (Figure 2b-f), with the (0 0 1) lattice plane normal parallel to, and the (3 1 0) plane normal perpendicular to, the long axis. Particle size distribution analysis (200 particles) revealed an average long-axis dimension of 89 ± 39 nm and aspect ratio 1.8 ± 0.7. Given the small aspect ratio of this sample, the relative sharpness of the (0 0 1) and (0 0 2) diffraction peaks suggested increased disorder within the atomic arrangement within *ab* planes relative to the stacking order along the *c*-axis, i.e. the (*h k* 0) diffraction peaks were disproportionately broadened in comparison to the (0 0 *l*) peaks. As diffusion is expected to occur in the *ab* plane,[36] the shortened diffusion distances resulting from the particle morphology should favor Mg^{2+} intercalation into the $V_4Nb_{18}O_{55}$ lattice. EDS analysis confirmed the expected homogenous distribution of V and Nb ions throughout the $V_4Nb_{18}O_{55}$ particle (Figure S5), and a V:Nb ratio of ca. 4:18 (Figure S6).

Evaluation of the electrochemical properties of $V_4Nb_{18}O_{55}$ was conducted at 110°C in a cell with a Mg^{2+} ionic liquid electrolyte against an activated carbon cloth (ACC) counterelectrode (Figure 3). The electrolyte, 0.5 M $Mg(TFSI)_2$ in $PY_{14}TFSI$, was chosen as it has the greatest stability at cathodic potentials of all known Mg-containing electrolytes (with minimal degradation observed in the range −1.7 V and 1.2 V vs carbon which corresponds to 0.5 V and 3.4 V vs Mg/Mg^{2+}),[28] and therefore, the observed cathodic electrochemistry was easier to attribute to cathodic activity as opposed to electrolyte decomposition. A cycling temperature of 110°C was chosen as oxides typically only intercalate significant Mg at elevated temperatures, i.e. 50°C or 110°C.[14,50]

The discharge behavior to the limit of the voltage stability window (represented by a blue line in Figure 3a and in Figure S3c) revealed two distinct regions of activity; a sloping plateau in the range 2.3 to 1.6 V vs Mg/Mg^{2+}, followed by a region of increasing capacity with further reduction in potential to 0.7 V vs Mg/Mg^{2+} (Figure 3a, S3c). dQ/dV analysis (Figure 3b) revealed that at least three distinct chemical processes occurred during charge; a higher potential redox couple centered at ~2.6 V vs Mg/Mg^{2+}, and two overlapping redox couples centered at ~1.4 V vs Mg/Mg^{2+}. The presence of the latter dual redox couple was revealed by a double peak in the charge cycle (found in the range 2.0 to 2.5 V vs. Mg/Mg^{2+}), which is not evident in the discharge peak below 1.5 V vs Mg/Mg^{2+} due to overlapping peak locations and possible concurrent electrolyte decomposition. Cycling in this range proved reasonably reversible, with 67% capacity retention over 50 cycles (Figure 3c). The large

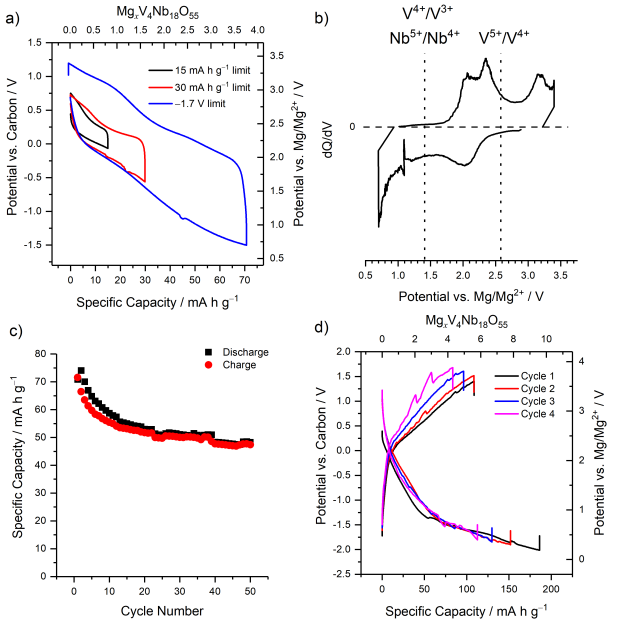

Figure 3. a) The discharge behavior for the first cycle of each depth of discharge, highlighting the increase in overpotential with depth of discharge (mass loading of electrode was 3.0 mg cm^{-2}) b) dQ/dV plot of the first full cycle with a −1.7 V voltage limit vs. ACC on the discharge. c) Capacity of discharge and charge vs cycle number for the −1.7 V vs. ACC discharge limit, using the same electrode as in a). d) Voltage vs Capacity for four cycles to a lower voltage limit of −2.5 V vs. ACC (mass loading of electrode was 2.8 mg cm^{-2}).

overpotentials observed with cycling across the electrolyte stability window (ca. 1.12 V) could be reduced significantly by limiting capacity to 15 and 30 mA h g^{-1}, (giving overpotentials of 0.33 and 0.47 V respectively, see Figure 3a and Figure S3a-b), which compares extremely favorably with other oxide materials (>0.8 V or higher).[28] This gave a round-trip energy efficiency of 81%, which is the highest observed for oxide materials in Mg batteries (Table 1) where Mg intercalation is proven by structural, redox, and elemental analysis. When a discharge limit beyond the electrolyte stability window was used (−2.5 V vs. ACC, Figure 3d), the measured capacity increased significantly (initial discharge capacity of 186 mA h g^{-1}). However, this capacity proved much less reversible and decreased to 113 mA h g^{-1} by the 4th cycle. The discharge capacity was consistently higher than the charge capacity (108 mA h g^{-1} on the first cycle) for these deep discharge tests, which suggested irreversible electrolyte decomposition was responsible for the capacity observed at these low potentials (<0.7 V vs Mg/Mg^{2+}) .Comparison with literature reports revealed the Mg-ion behavior of $V_4Nb_{18}O_{55}$ corresponded well to its Li-ion behavior; in Li-ion, the redox processes occurred at ~3.0 V and ~1.75 V vs Li/Li$^+$, respectively, thereby possessing a similar redox potential separation (~1.2 V).[38] These processes are attributed to the V^{5+}/V^{4+} couple and a combination of the V^{4+}/V^{3+} and Nb^{5+}/Nb^{4+} couples, respectively, as indicated by three peak maxima within the charge process (only two were visible on the discharge as the lowest discharge maxima is not reached within the cycling window, and the V^{4+}/V^{3+} and Nb^{5+}/Nb^{4+} couples overlap. These redox changes are corroborated with XAS analysis below.

Five electrodes of the material were recovered following electrochemical discharge (Mg insertion), or electrochemical discharge and charge (Mg insertion and removal) as described in the Experimental section. These were labelled "VNO(Discharged_*x*)" (*x* = 1, 2 or 3) and "VNO(Charged_*y*)" (y = 1 or 2) respectively, and their electrochemistries are shown in Figure S4. While voltage plateaus were occasionally observed consistent with electrolyte degradation, they provided useful insights into both structural and redox changes in $V_4Nb_{18}O_{55}$ with cycling when analyzed by a combination of EDX, XRD and XAS analysis. The observed Mg:Nb ion ratios within VNO(Discharged_1) from EDX were 4:18, which corresponded well to the predicted stoichiometry ($Mg_{3.5}V_4Nb_{18}O_{55}$) from the observed discharged capacity (68 mA h g^{-1}), and given the low H_2O content of the electrolyte, this suggested Mg intercalation (rather than proton intercalation) had indeed taken place. HAADF-STEM and EDX mapping of VNO(Discharged_2) confirmed a uniform dispersion of Mg (ions) found within the particles, consistent with predominant insertion vis-à-vis surface reactivity with the electrolyte (Figure S10). Conversely for VNO(Charged_1) and VNO(Charged_2), the observed Mg:Nb ratios were 0.81:18 and 0.13:18, respectively. This observation suggested a limited proportion of Mg was irreversibly trapped in the active material of the respective electrodes, although this could be somewhat reduced when the electrode was overcharged in the case of VNO(Charged_2).

A comparison of the XRD patterns of the pristine, discharged and charged materials provided further strong evidence for Mg^{2+} intercalation behavior (Figure 4). While the exact nature of the shifts were not obvious on inspection of the (0 0 1) peak (Figure 4b) due to zero errors, peak broadening and anisotropy effects, LeBail fitting (which incorporates all diffraction peaks and accounts for these additional effects) revealed that VNO(Discharged_2) displayed an anisotropic expansion of the lattice parameters, with the largest increase in the *b* parameter, and a ~1% increase in unit cell volume overall, as indicated by the shift to lower scattering vector in the discharged electrode (Table 2 and

Table 2. The lattice parameters and their standard errors calculated from LeBail refinement for the pristine sample, and the electrodes VNO(Discharged_2), VNO(Charged_1) and VNO(Charged_2).

	a / Å	Δ*a* / %	*b* / Å	Δ*b* / %	*c* / Å	Δ*c* / %	*V* / Å^3	Δ*V* / %	R_{wp}
Pristine	17.3658(12)	-	17.6500(14)	-	3.97886(6)	-	1219.55(13)	-	7.80
VNO(Discharged_2)	17.4045(9)	0.22	17.7385(9)	0.50	3.99242(4)	0.34	1232.58(10)	1.07	8.47
VNO(Charged_1)	17.404(2)	0.22	17.674(2)	0.14	3.9859(3)	0.18	1226.0(2)	0.53	9.44
VNO(Charged_2)	17.403(4)	0.21	17.653(5)	0.02	3.9851(4)	0.16	1224.3(5)	0.39	3.25

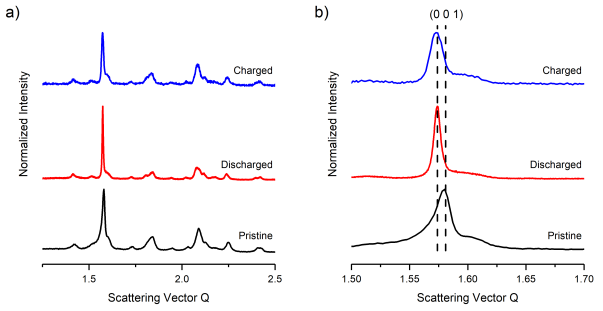

Figure 4. a) XRD patterns of the pristine, discharged and charged materials, VNO(Discharged_2) and VNO(Charged_2) respectively. b) a comparison of the (0 0 1) diffraction peak of the pristine and charged materials, revealing a small shift in diffraction peak location.

Figure 4). Partial removal of Mg^{2+} was suggested by the unit cell unit cell volume almost exactly half-way in between VNO(Discharged_2) and the pristine sample. VNO(Charged_2) demonstrated greatest similarity with the pristine sample, implying further (but not complete) Mg removal with overcharging (the XRD pattern of VNO(Charged_1) is shown in the SI). Interestingly, the *b* parameter was returned to its original value with over-charging, whereas the changes in *a* and *c* were largely irreversible, respectively. This suggested that Mg^{2+} was primarily trapped in crystallographic sites which distorted these specific parameters. Rietveld refinement of the discharged and charged electrodes was attempted using the predicted magnesiated structures from the DFT analysis (discussed later); however, the differences in diffraction pattern peak intensities with Mg inclusion were so minimal, Mg location (and any potential defect formation) could not be extracted with any confidence. Moreover, the peak broadening evident in the discharged and charged states (Figure 4a) relative to the pristine sample suggested some loss of crystallinity, or crystallographic strain, with Mg intercalation. Therefore, local structure methodologies, such as pair distribution function (PDF), are suggested in further studies to accurately determine Mg site occupancies in this material.

To determine the effect of Mg insertion on elemental oxidation states, XAS analysis was conducted on pristine $V_4Nb_{18}O_{55}$, and electrodes VNO(Discharged_1) and VNO(Charged_2) on the V $L_{2,3}$-, O K, and Nb L_3-edges. Additionally, V and Nb K-edge data were collected for the pristine compounds, and is discussed in the SI. XAS data was collected using both total electron and fluorescence yield detectors. Signals from electron yields correspond to the chemical state of the surface layer of the material, whereas fluorescence yields correspond to approximately 100 nm into the electrode, thus having a notable contribution from the bulk crystal structure, especially considering the particle size of the materials. Comparison between electron yield and fluorescence yields therefore allowed for the distinction between bulk and surface reactions with Mg insertion/removal. The V $L_{2,3}$-edge spectra of V_2O_5 and pristine $V_4Nb_{18}O_{55}$ were similar in shape and position in both electron and fluorescence excited electron transitions from the vanadium core $2p_{3/2}$(L_3) and $2p_{1/2}$ (L_2) levels to unoccupied

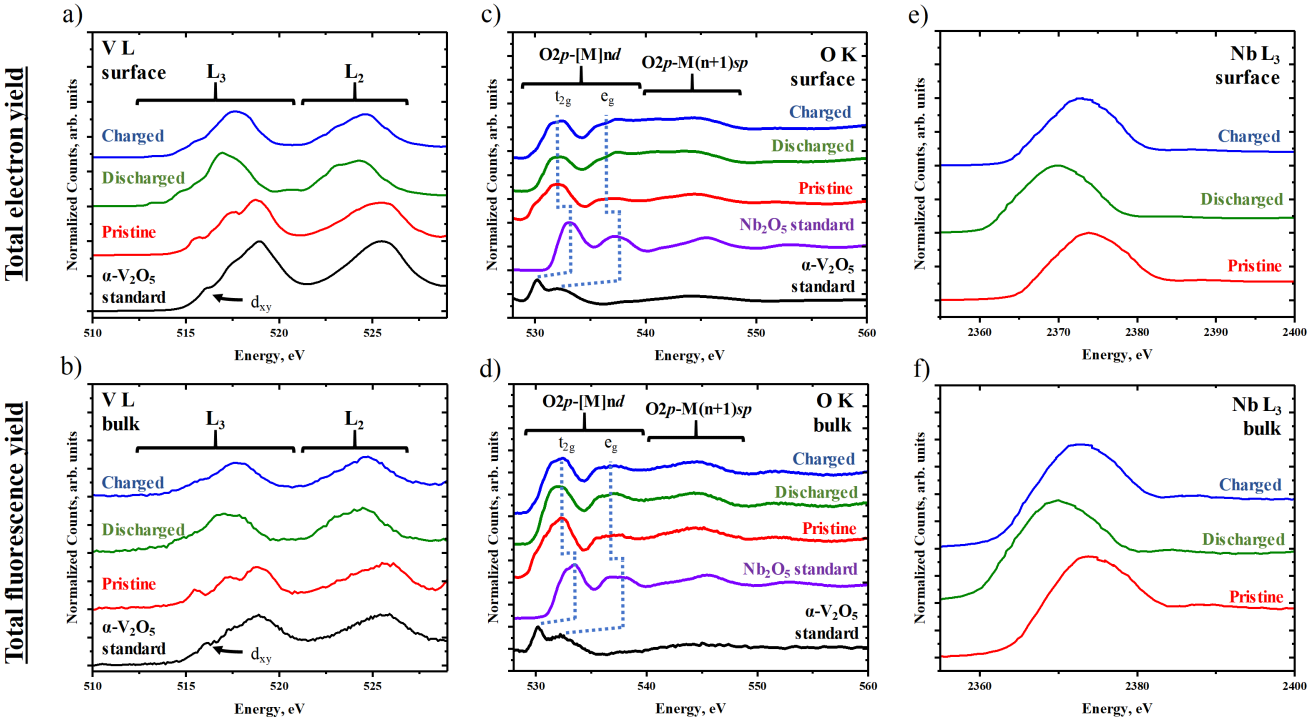

Figure 5. Integrated X-ray absorption spectra of the V $L_{2,3}$ (a,b), O K (c,d), and Nb L_3 (e,f) edges of pristine $V_4Nb_{18}O_{55}$, discharged to −1.7 V and charged VNO. Standards of orthorhombic V_2O_5 and Nb_2O_5 are shown. Electron yields, corresponding to surface chemistry, of each edge are on top (a,c,e). Fluorescence yields, corresponding to bulk properties, of each edge are on the bottom (b,d,f).

V 3d states. These results provide evidence that V was in the 5+ oxidation state throughout the $V_4Nb_{18}O_{55}$ particles, i.e. both on the surface and in the bulk.[14,37,50–55] This conclusion was supported by the measurements at the V K-edge in transmission mode, and detailed discussion of these spectra is included in the SI.[50,52,53,56] Upon discharge to −1.7 V vs ACC, the L_3 and L_2 features were generally red-shifted and changed shape, and spectra collected in electron and fluorescent yields were similar. The maximum intensity in the L_3 region was at 517 eV, with additional, less intense features at 513 eV, 518 eV and 521 eV.

In turn, the L_2 spectrum broadened through the appearance of two maxima at 523.5 and 524.2 eV. Overall, the spectra for discharged $V_4Nb_{18}O_{55}$ matched theoretical and experimental reports on compounds containing V^{3+} in distorted $[VO_6]$ octahedra, both at the surface and within the bulk of the electrode.[25,50,52,53] This observation was consistent with Mg^{2+} intercalation into $V_4Nb_{18}O_{55}$, in agreement with electrochemical, microscopic and structural analysis. Upon charging, the region of maximum intensity of the L_3-edge broadened, and the maximum blue-shifted to ca. 518 eV in electron and fluorescence yields. Also, the broad doublet was lost in the L_2 region, leading to a single maximum slightly above 524 eV, thereby blue-shifting the center of gravity. These changes were indicative of electrochemical oxidation of V to 4+.[14,25] This means that reduction of V^{5+} to V^{3+} upon discharge was not completely reversible, and further confirmed incomplete removal of Mg upon charge.

Figure 5c,d depicts integrated O K-edge X-ray absorption spectra acquired for pristine and electrochemically tested $V_4Nb_{18}O_{55}$ samples, the spectra for V_2O_5 and Nb_2O_5 are depicted alongside for comparison. The O K-edge features resulted from excited electron transitions from the core O 1s levels to unoccupied O 2p states that hybridized with metal states.[57] Within the O K-edge of pristine $V_4Nb_{18}O_{55}$, two broad spectral events occurred at ca. 532 and 537 eV. The absorption events below 540 eV corresponded to O 2p states that hybridized with V 3d and Nb 4d states. The first event (532 eV) was very broad with a band dispersion (FWHM) of 4 eV and appears to result from contributions from t_{2g} and e_g states from $[VO_n]$ moieties and t_{2g} of $[NbO6]$ octahedra, based on comparison with the respective standards.[57] The second event (537 eV) matched with the spectrum of Nb_2O_5, suggesting that it arose solely from the e_g states of $[NbO_6]$ in the structure. Above 540 eV, O 2p states hybridized with V 4sp and Nb 5sp states. The center of gravity of the t_{2g} event of pristine $V_4Nb_{18}O_{55}$ was greater than the t_{2g} event of V_2O_5 and less than the t_{2g} event of Nb_2O_5. This is expected because the O 1s absorption threshold blue-shifts with increasing atomic number.[57] Additionally, the energy separation of t_{2g} and e_g states increased with atomic number. In both electron and fluorescence yields of figure 5c,d one feature was centered at 545 eV in the O 2p-M (n+1)sp region for pristine $V_4Nb_{18}O_{55}$. This was again in good correspondence with the addition of features from both V_2O_5 and Nb_2O_5. The similarity between sample and the standards was consistent with a similar metal-oxygen coordination and covalent interactions in these compounds. Upon discharge of the cell to −1.7 V vs. ACC, the dispersion of the features at ~532 eV red-shifted by 2 eV and the center of gravity shifted to higher energy for both electron and fluorescence yields. This observation corresponded to occupation of the first states just above the Fermi level through reduction of the metal-oxygen bonds. Correspondingly, the O 2p-M (n+1)sp red-shifted by ca. 1 eV upon discharge, consistent with a decrease of the binding energy of the core electrons when the compound was reduced. Upon charge, the t_{2g} spectral event changed shape as the higher energy shoulder raised slightly for both electron and fluorescence yields, but did not change position (Figure S12). The rest of the spectra changed only subtly. The fact that the spectrum did not return to the pristine state indicated chemical irreversibility, consistent with V $L_{2,3}$-edge observations. Figure 5e-f depicts the Nb L_3-edge in electron and fluorescence yields. The L_3 edge of pristine $V_4Nb_{18}O_{55}$ displayed a prominent absorption event with a maximum at 2373.8 eV, followed by a weak event at ca. 2388 eV in both electron and fluorescence yields, similar to Nb^{5+} standards in references 51 and 52. The strong peak is associated with electron transitions from Nb core $2p_{3/2}$ to unoccupied 4d states and the weak peak is associated with Nb $2p_{3/2}$ to 5s transitions.[58,59] These results provide evidence that Nb was in the 5+ oxidation state on the surface and in the bulk of pristine $V_4Nb_{18}O_{55}$. This conclusion was supported by the measurements at the Nb K-edge in transmission mode, showing that the oxidation state of Nb in pristine $V_4Nb_{18}O_{55}$ was 5+ throughout the particle (Figure S11). Further discussion of Nb K-edge spectra of pristine $V_4Nb_{18}O_{55}$ is in the SI.[58–61] Upon discharge, the Nb L_3-edge did not change shape but red-shifted by −3.7 eV in both electron and fluorescence yields, consistent with Nb reduction.[58,69] Upon charging, the Nb L_3-edge blue-shifted by +3 eV in both electron and fluorescence yields. The change confirms that Nb re-oxidized, but did not completely urn to the pristine state, indicating that the electrochemistry is not completely reversible. No evidence existed of chemical gradients (or different oxidation states) between surface and bulk at this edge, based on comparison of data from the two detectors employed, consistent with bulk (rather than surface) reactivity.

Hybrid-exchange DFT calculations were performed to investigate the electronic and structural properties of $V_4Nb_{18}O_{55}$ (full details in the SI). As previously discussed, the structure contains partially occupied V sites on the oxygen-rich 'B' plane. To represent this key structural feature, but keep the unit cell size within computational limits, two models were constructed based upon the crystallographic (*C*) and primitive (*P*) unit cells, giving stoichiometries of $V_4Nb_{22}O_{65}$ and $V_3Nb_{11}O_{34}$ (details in the SI).

These models gave a representation of a closed-shell system (*C*, containing only d^0 cations) and an O-deficient system (*P*, containing unpaired electrons) respectively. The latter model was useful to consider, since reduced metal centers are known to occur in similar bronze-type frameworks containing V and Mo.[37] The calculated lattice parameters of the

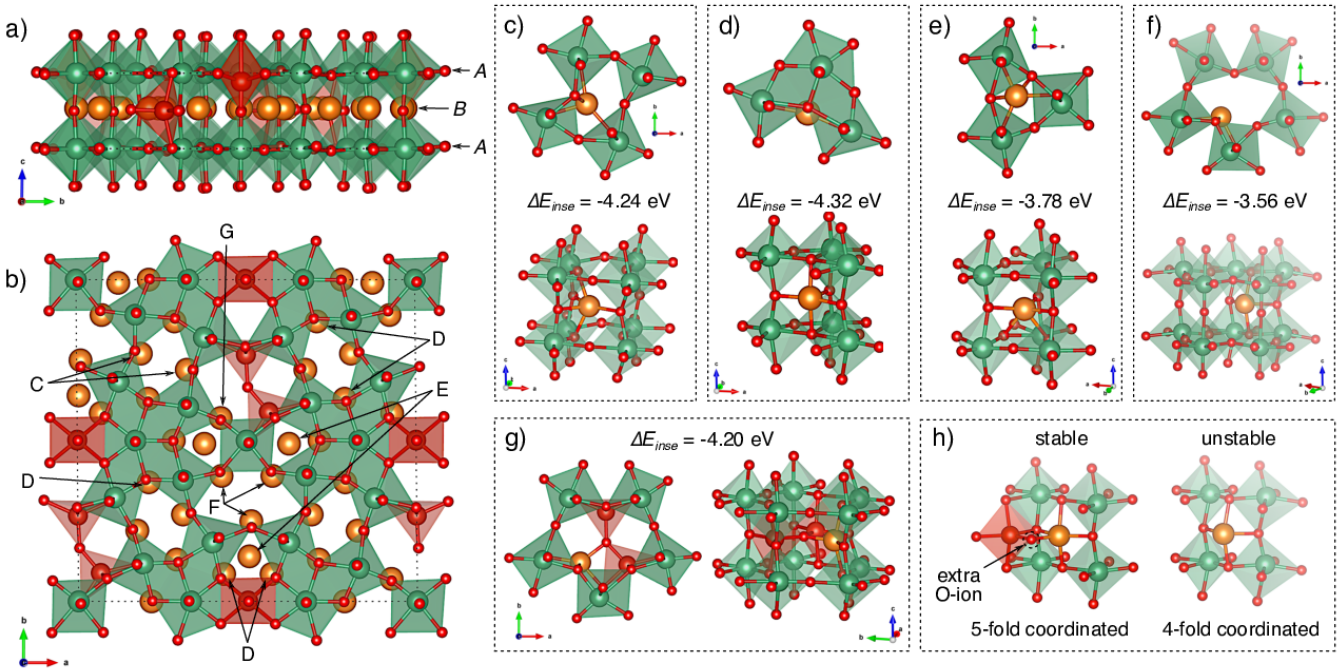

Figure 6. Structure of $V_4Nb_{18}O_{55}$ (shown as the P cell model, with stoichiometry $V_3Nb_{11}O_{33}$) viewed along a) the *a* axis, highlighting the metal rich A and oxygen rich B planes and b) viewed along the 'tunnel' *c* axis. Gold spheres indicate stable sites for Mg, grouped according to their similar local geometry, labeled C-G. Optimized geometry of Mg ions in sites C-G are indicated in parts c) – g), viewed along both the *c* axis, and in the ab plane perspective. The insertion energy of the sites relative to Mg metal is shown. h) The relationship between Mg ion site stability and the coordination number it can achieve.

two DFT models are reported in Table 3 and showed good agreement with the literature values, despite the deviation from experimental stoichiometry in each case.

A range of insertion sites for Mg-ions were investigated in the primitive cell model. The calculations revealed that Mg always occupied sites on the oxygen-rich *B* plane (Figure 6a). Mg-ions introduced onto the *A* plane always found stable locations on the *B* plane, minimizing their Coulombic repulsion from structural Nb and V cations. Figure 6b shows insertion sites for Mg-ions in the *P* cell, grouped together according to their local geometry, and labelled C-G. Figures 6c-g show representative optimized structures for the different sites, indicating their local geometry and calculated insertion energy (ΔE_{inse}) vs. Mg metal. The most stable sites for Mg-ions were C and D, located in the 4-membered rings (Figures 6c,d). In these sites, Mg-ions could achieve coordination to 5 neighboring oxyanions. There were two possible local environments for Mg-ions occupying D sites; those with only Nb neighbors, which are more stable, and those with Nb and V neighbors, which were destabilized by ~0.3 eV. Mg-ions could occupy E sites in the 3-membered rings (Figure 6f), which were slightly destabilized with respect to C and D sites by ~0.4 eV. Mg-ions occupying F sites in the 5-membered rings (Figure 6f) were the least stable locations, destabilized by ~0.75 eV compared to C and D sites. The final possible insertion site was G, indicated in Figure 9g, where an Mg-ion occupied a site in the 5-membered ring, which was also occupied by interlayer V-ions. G sites were stabilized by 0.65 eV compared to F sites. In G sites, the Mg-ion could form a bond with the O-ion bridging between the V ions (Figure 6h), resulting in a stable 5-fold coordination, unlike F sites, where the Mg-ion could achieve only an unfavorable 4-fold coordination. The ability of Mg to coordinate to either 5 or 4 O-ions was therefore a key factor determining the stability in different insertion sites.

The diffusion pathways between the sites identified in Figure 6 were evaluated with DFT. Due to the complex structure of the material, and the number of local minima that Mg^{2+} may occupy, investigating all possible pathways for Mg migration in a unit cell was impractical. Therefore, to gain an understanding of Mg mobility in $V_4Nb_{18}O_{55}$, a selection of pathways was chosen to give a representative behavior in proximity to different structural motifs, and provide a percolating route demonstrating that migration can occur throughout the structure. Figure 7 a) – h) shows the calculated activation barriers for the selected routes, starting from a stable D site. Mg migration could occur between low energy C and D sites in the 4-membered rings with low activation barriers in the range 0.14 to 0.61 eV (Figures 7a,g). However, for Mg-ions to migrate into the less stable F sites (in the 5-membered rings), higher barriers existed in the range 0.92 to 1.05 eV (Figures 7b,d). Similarly, moving between F sites had high barriers in the range 0.69 to 0.82 eV. Mg mobility through the empty 5-membered rings, into and between F sites, was therefore kinetically hindered. However, when the 5-membered rings were occupied with interlayer V ions, Mg could migrate into G sites, in which the Mg-ions were stabilized by the additional neighboring oxyanion to achieve a more favorable 5-fold coordination (Figure 7g,h). This stabilization provided lower energy barriers

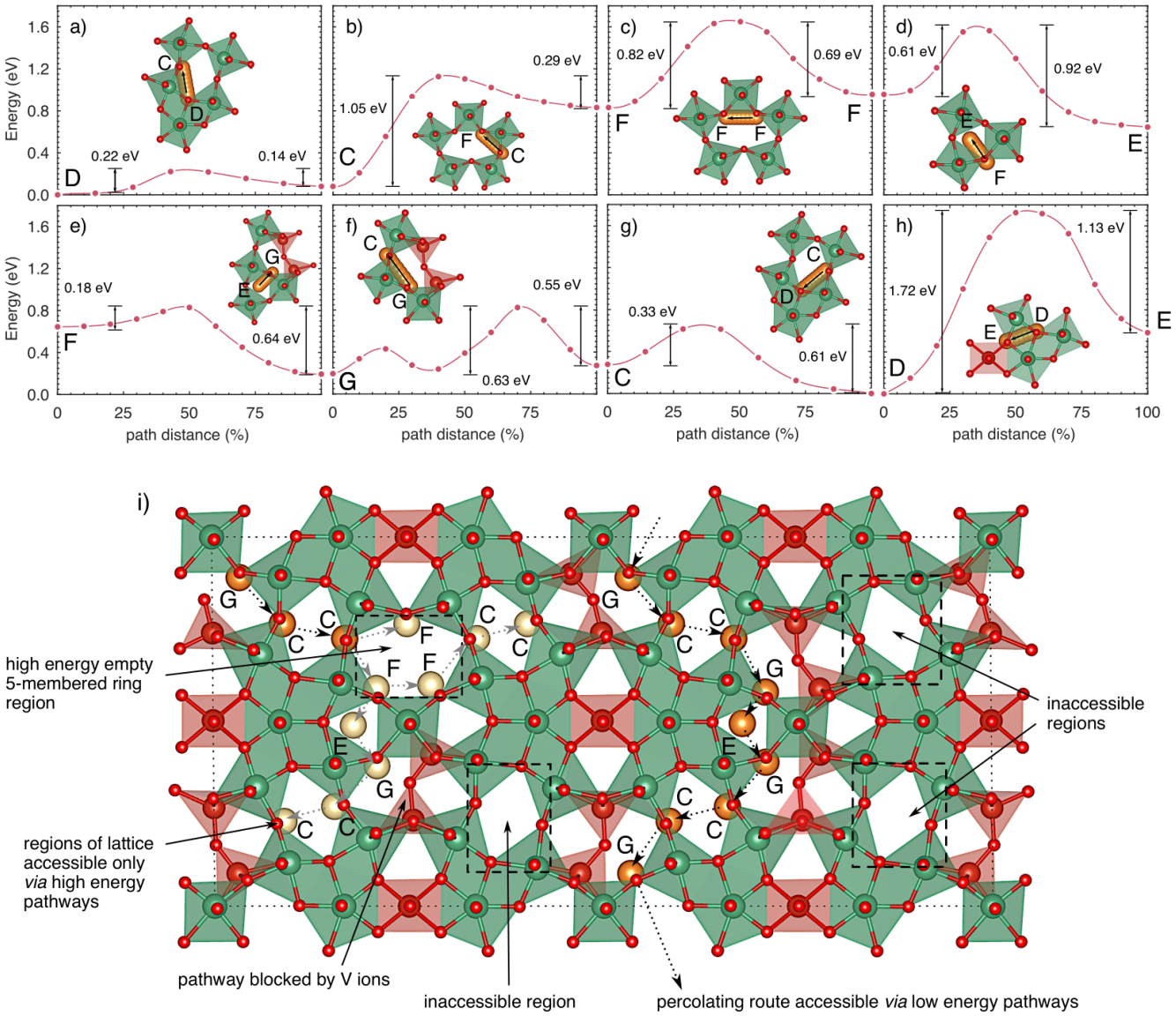

Figure 7. a) – h) Calculated activation barriers for Mg diffusion through the $V_4Nb_{18}O_{55}$ lattice. Energies are plotted in a consistent reference frame due to the percolating nature of the pathways investigated, with activation barriers for forward and backward migration indicated on each plot. The local geometry of the corresponding migration pathways are shown inset. i) Migration routes throughout the structure using low (black dotted arrows) and high energy (grey dotted arrows) pathways. Gold spheres indicate Mg sites accessible via low energy pathways a), e), f) and g). White spheres indicate Mg sites accessible only via high energy pathways b) c) and d) by crossing empty 5-membered ring regions. Green and large red spheres indicate Nb and V, respectively, whereas small red spheres correspond to O.

in the range 0.55 to 0.63 eV for Mg migration through G sites (Figure 7f), compared to when the 5-membered rings were unoccupied (F sites). As the interlayer V ions in these fractionally occupied sites are disordered through the lattice, and can be arranged in one of two configurations (Figure 6f,g), they could either facilitate migration of Mg, or block migration pathways. It was only when neighboring 5-membered ring were occupied by V ions in a suitable configuration that Mg-ions could migrate through the structure along low energy percolating pathways with a maximum activation barrier of ~0.65 eV, using a combination of routes indicated in Figures 7 a), e), f) and g). The arrangement of the interlayer V ions may be such that pathways were blocked, and regions of the lattice inaccessible to migrating Mg-ions. An illustration of these two situations is provided in Figure 7i. We also note that Mg migration across the shared edge of $NbO_{6/7}$ units (Figure 7h) had a high barrier of ~1.72 eV and these pathways were inaccessible. For Mg-ions to access a higher fraction of the lattice, passage through destabilized F sites in empty 5-membered rings, with higher energy barriers, is required.

Table 3. The lattice parameters for $V_4Nb_{18}O_{55}$ from the DFT models and the LeBail refinement of the experimental material, compared with the previously reported values from literature.

	Stoichiometry	a (Å)	Δa	b (Å)	Δb	c (Å)	Δc
Börrnert et al.	$V_4Nb_{18}O_{55}$	17.355	-	17.698	-	3.971	-
C	$V_4Nb_{22}O_{65}$	17.3918	0.2%	18.0077	1.7%	3.9748	0.1%
P	$V_3Nb_{11}O_{34}$	17.5097	0.9%	17.9076	1.2%	4.0013	0.8%
This work	$V_4Nb_{18}O_{55}$	17.3658	0.06%	17.6500	–0.3%	3.9789	0.2%
This work	$Mg_{3.5}V_4Nb_{18}O_{55}$	17.4045	0.3%	17.7385	0.2%	3.9924	0.5%

In the present case, for Mg-ions to penetrate the center of the $V_4Nb_{18}O_{55}$ particles, they must travel along a diffusion length (L) which can be estimated to be ~25 nm, corresponding to half the distance along the *ab* plane for the $V_4Nb_{18}O_{55}$ rods in this study (~50 nm width). The diffusion length L scales with $\sqrt{\boldsymbol{Dt}}$, where D is the diffusivity and t is the discharge time (in this case 3 h, corresponding to a rate of C/3 or 15 mA g^{-1} as used in the electrochemical experiments). Therefore, a diffusivity of ~5.8×10^{-20} m^2 s^{-1} is required for Mg insertion to the center of a $V_4Nb_{18}O_{55}$ particle during discharge. The diffusivity D can be approximated using:

$$\boldsymbol{D} \approx \boldsymbol{\nu} \cdot \boldsymbol{a}^2 \cdot \exp\left(\frac{-\boldsymbol{E_m}}{\boldsymbol{kT}}\right)$$

Where $\boldsymbol{\nu}$ is the atomic jump frequency, and $\boldsymbol{a}$ is the jump distance. If we assume reasonable values of $\boldsymbol{\nu}$ = 10^{12} s^{-1} and $\boldsymbol{a}$ = 3 Å,[40] the maximum tolerable activation barrier is ~720 meV at 25 °C (298.15 K), and 930 meV at the elevated temperature used in this study (110 °C). These computational results provide a framework for rationalizing the electrochemical observations in Figure 5. The low overpotentials observed for shallow charge/discharge cycles may correspond to Mg migration through the regions of the structure accessible along low energy pathways with barriers of up to ~650 meV. Much of the structure will, however, be inaccessible for Mg in this way. This is due to the low fraction (~0.35) of 5-membered rings occupied by VO_5 units, some of which will block Mg mobility rather than facilitate it. Under these shallow discharge conditions, and limited regions of the structure accessible, a low capacity was expected, in agreement with the 15 - 30 mA h g^{-1} achieved. Under deeper discharge conditions at elevated temperatures, Mg-ions may be able to pass through kinetically limited high-energy regions of unoccupied 5-membered rings, with higher barriers in the range 0.92 – 1.05 eV for mobility. Under these conditions, we would expect Mg to access a greater proportion of the structure and thus provide a higher capacity, but at the cost of significantly increased overpotentials, as is observed experimentally. We note that Mg-ions may be retained in stable locations in the structure under these deep cycling conditions, which would result in capacity fade and irreversible crystallographic changes within the $V_4Nb_{18}O_{55}$ structure.

While we saw no evidence of conversion reactions taking place during cycling, we performed DFT calculations following the approach detailed in Hanna *et al.* to calculate voltages for intercalation (V_{int}) and conversion (V_{conv}) and thereby assess the relative favorability of both reaction pathways.[63] The competing reactions in this case can be defined as:

$$xMg_{(s)} + V_4Nb_{18}O_{55} \rightarrow Mg_xV_4Nb_{18}O_{55}\ (intercalation)$$

$$xMg_{(s)} + V_4Nb_{18}O_{55} \rightarrow xMgO + \sum conversion\ products\ \ (conversion)$$

and the calculated voltages can be determined by as:

$$V_{int} = -\frac{G_{Mg_xV_4Nb_{22}O_{65}} - G_{xMg_{(s)}} - G_{V_4Nb_{22}O_{65}}}{zF}$$

and

$$V_{conv} = -\frac{\sum_i G_i^{conv} - G_{xMg_{(s)}} - G_{V_4Nb_{22}O_{65}}}{zF}$$

where

$$\sum_i G_i^{conv}$$

is the sum of the conversion products, containing x moles of MgO. G is the Gibbs free energy, which can be reasonably approximated by the 0 K enthalpies obtained from the calculations. Since there is no experimental suggestion of the potential conversion products, we considered the reduced oxides V_2O_3 and NbO_2, given the lowest oxidation states for V and Nb were 3+ and 4+, respectively, in discharged $V_4Nb_{18}O_{55}$ from XAS analysis.

Our DFT calculations necessitated the use of an off-stoichiometric model of the conventional unit cell to account for the disorder of V ions in the 5-membered rings in the real material. We used a cell with composition $V_4Nb_{22}O_{65}$. The approximate composition of the discharged electrode is $Mg_4V_4Nb_{18}O_{55}$. We therefore chose to investigate the difference in conversion vs intercalation voltages at stoichiometries of $MgV_4Nb_{22}O_{65}$ and $Mg_4V_4Nb_{22}O_{65}$.For $MgV_4Nb_{22}O_{65}$ the potential to form conversion products was calculated to be:

$$V_{conv}\left[Mg_{(s)} + V_4Nb_{22}O_{65} \rightarrow MgO + 2V_2O_5 + 10Nb_2O_5 + 2NbO_2\right] = 1.98\ V$$

and the intercalation voltage was:

$$V_{int}\left[Mg_{(s)} + V_4Nb_{22}O_{65} \rightarrow MgV_4Nb_{22}O_{65}\right] = 2.16\ V$$

Therefore, intercalation is thermodynamically favoured in this case. For the electrode discharged to a stoichiometry of $Mg_4V_4Nb_{22}O_{65}$, we can calculate pathways to two difference sets of conversion products:

$$V_{conv}\left[4Mg_{(s)} + V_4Nb_{22}O_{65} \rightarrow 4MgO + 2V_2O_3 + 11Nb_2O_5\right] = 1.27\ V$$

$$V_{conv}\left[4Mg_{(s)} + V_4Nb_{22}O_{65} \rightarrow 4MgO + 2V_2O_5 + 7Nb_2O_5 + 8NbO_2\right] = 1.95\ V$$

and the competing intercalation reaction is:

$$V_{int}\left[4Mg_{(s)} + V_4Nb_{22}O_{65} \rightarrow Mg_4V_4Nb_{22}O_{65}\right] = 1.81\ V$$

In this case, the conversion reaction is slightly thermodynamically favoured over intercalation, but only by 0.16 V. Considering the thermodynamic driving force for conversion is small, the $V_4Nb_{18}O_{55}$ structure is expected to show high kinetic stability, and there is no evidence from experiment for conversion products such as MgO, V_2O_3, Nb_2O_5 and NbO_2, we can exclude significant conversion reactions from taking place.

Overall, these DFT results suggested that bronze-type frameworks can be used to achieve good Mg^{2+} migration in oxide materials, but diffusion is highly dependent on local coordination geometry of the migrating Mg^{2+}. Considering the above discussion, we can suggest some preliminary design rules for Mg-ion mobility in bronze-type structures. Frameworks containing 5-membered rings should be avoided, since these provide regions limiting Mg mobility. Since the instability of the Mg-ions can be assigned to the unfavorable 4-fold coordination they achieve in the 5-membered ring windows (Figure 6f,h), it follows that larger rings (i.e. 6 and 7-membered) will be similarly unfavorable regions for Mg to occupy and traverse. Structures comprised of only 3 and 4-membered rings are therefore expected to provide more favorable energy pathways. An alternative strategy to achieve enhanced Mg mobility can be deduced from the facilitation of migration through the 5-membered rings by the VO_5 units. The geometry of these interlayer V ions offers an additional O-ion coordination site for the migrating Mg, and provide stabilization. The use of extra-framework, interstitial or mobile O-ions may therefore provide a strategy for enhancing Mg-ion mobility. It should be noted that the observed experimental kinetics for Mg intercalation in $V_4Nb_{18}O_{55}$ are still relatively inhibited in comparison to Mo_6S_8, despite possessing similar computed activation energy values (0.65 eV vs 0.44-0.51 eV respectively),[61] suggesting that other limiting factors, such as transfer from the electrolyte to the electrode, present kinetic barriers in oxide electrode magnesiation.

Conclusions

The tetragonal tungsten bronze $V_4Nb_{18}O_{55}$ was evaluated as a member of a new class of Mg-ion intercalation hosts for Mg batteries. Partially reversible Mg-ion insertion was achieved at 110 °C, with a maximum capacity of 75 mA h g^{-1}, corresponding to 4 Mg^{2+} ions per formula unit. The electrochemical response could be sustained at moderate efficiency over tens of cycles, indicating some reversibility. The insertion and partial removal of Mg was corroborated with elemental, crystallographic, and spectroscopic methodologies. Powder X-ray diffraction revealed crystal lattice expansion on Mg insertion, whilst X-ray absorption spectroscopy showed reduction of V^{5+} to V^{3+} and partial reduction of Nb^{5+} to Nb^{4+} upon discharge. These changes were shown to be partially reversed upon charge, suggesting some irreversible Mg insertion, consistent with the electrochemical measurements. DFT calculations and analysis suggested the structure of $V_4Nb_{18}O_{55}$ facilitates relatively rapid Mg^{2+} diffusion along the *ab* crystallographic plane. Therefore, it is suggested that other tetragonal tungsten bronze frameworks may hold promise as Mg electrode materials in the future.

ASSOCIATED CONTENT

Supporting information. V^{4+} solution synthesis protocol, Continuous Hydrothermal Flow Synthesis apparatus, LeBail refinement plots, electrochemical figures, EDX analysis, XAS analysis, DFT computational methodology. This material is available free of charge via the Internet at http://pubs.acs.org.

AUTHOR INFORMATION

Corresponding Authors

*Professor Jawwad Darr
Department of Chemistry
University College London
20 Gower Street, London
WC1H 0AJ
UK
Tel: +44 (0)20 7679 4312.
e-mail: j.a.darr@ucl.ac.uk

*Professor Jordi Cabana
Department of Chemistry
University of Illinois at Chicago
Chicago
IL 60607
USA
Tel: (+1) 312-355-4309 . email: jcabana@uic.edu

Author Contributions

‡ The contribution of IDJ and GN to this work was equal. IDJ and GN co-wrote the manuscript. IDJ, GN and HYD performed the electrochemical testing and analysis. IDJ and DT performed the synthesis of $V_4Nb_{18}O_{55}$. GN and JWF performed the XAS analysis. KM and FC performed the DFT analysis and interpretation. IDJ and JKC performed the XRD and LeBail analysis. YAW, LH and RFK performed the HAADF imaging and EDX measurements. JC, JAD and IPP edited the manuscript. JC is the academic lead of the Mg battery research team at the University of Illinois at Chicago. JAD is the academic lead of the synthesis team at University College London, and co-developed the CHFS process used within this work. All authors have given approval to the final version of the manuscript.

ACKNOWLEDGMENT

IDJ and JAD would like to thank the EPSRC for funding the JUICED project (EP/R023662/1). GN, YW, LH, HDY, RK and JC were supported as part of the Joint Center for Energy Storage Research (JCESR, a U.S. Department of Energy, Energy Innovation Hub). IDJ would also like to thank the Materials Modelling and Molecular Doctoral Training Centre (EP/G036675/1) and the STFC for providing funding support for travel within the collaboration (STFC/MDC Futures Early Career Award, ST/N002385/1). Use of the Advanced Photon Source was supported by the U.S. Department of Energy, Office of Science, under Contract No. DE-AC02-06CH11357. Additionally, we thank the Diamond Light Source for the award of beam time as part of the Energy Materials Block Allocation Group SP14239.

ABBREVIATIONS

ACC, activated carbon cloth; BPR, back-pressure regulator; CJM, confined jet mixer; CHFS, continuous hydrothermal flow synthesis; DFT, density functional theory; EDS, energy-dispersive X-ray spectroscopy; FWHM, full width at half maximum; HAADF-STEM, High-Angle Annular Dark-Field Scanning Transmission Electron Microscopy; ICSD, International Crystal Structure Database; $MgTFSI_2$-$PY_{14}TFSI$, $Mg[N(SO_2)_2(CF_3)_2)_2$-$(C_9H_{20}N)(N(SO_2)_2(CF_3)_2]$; NMP, N-methyl pyrrolidone; NMR, nuclear magnetic resonance; PDF, pair distribution function; PVDF, polyvinylidene difluoride; PXRD, powder X-ray diffraction; SDD, silicon drift detector; TEM, transmission electron microscopy; TEY, total electron yield; TFY, total fluorescence yield; XAS, X-ray Absorption Spectroscopy; XRD, X-ray diffraction.

REFERENCES

(1) Armand, M.; Tarascon, J.-M. Building Better Batteries. *Nature* **2008**, *451* (7179), 652–657. https://doi.org/10.1038/451652a.

(2) Whittingham, M. S. Ultimate Limits to Intercalation Reactions for Lithium Batteries. *Chem. Rev.* **2014**, *114* (23), 11414–11443. https://doi.org/10.1021/cr5003003.

(3) Ling, C.; Banerjee, D.; Matsui, M. Study of the Electrochemical Deposition of Mg in the Atomic Level: Why It Prefers the Non-Dendritic Morphology. *Electrochim. Acta* **2012**, *76*, 270–274. https://doi.org/10.1016/j.electacta.2012.05.001.

(4) Matsui, M. Study on Electrochemically Deposited Mg Metal. *J. Power Sources* **2011**, *196* (16), 7048–7055. https://doi.org/10.1016/j.jpowsour.2010.11.141.

(5) Takehara, Z. Future Prospects of the Lithium Metal Anode. *J. Power Sources* **1997**, *68* (1), 82–86. https://doi.org/10.1016/S0378-7753(96)02546-3.

(6) Canepa, P.; Sai Gautam, G.; Hannah, D. C.; Malik, R.; Liu, M.; Gallagher, K. G.; Persson, K. A.; Ceder, G. Odyssey of Multivalent Cathode Materials: Open Questions and Future Challenges. *Chem. Rev.* **2017**, *117* (5), 4287–4341. https://doi.org/10.1021/acs.chemrev.6b00614.

(7) It's Elemental - The Periodic Table of Elements https://education.jlab.org/itselemental/index.html (accessed Jul 26, 2019).

(8) Shannon, R. D. Revised Effective Ionic Radii and Systematic Studies of Interatomic Distances in Halides and Chalcogenides. *Acta Crystallogr. Sect. A* **1976**, *32* (5), 751–767. https://doi.org/10.1107/S0567739476001551.

(9) Levi, E.; Gofer, Y.; Aurbach, D. On the Way to Rechargeable Mg Batteries: The Challenge of New Cathode Materials. *Chem. Mater.* **2010**, *22* (3), 860–868. https://doi.org/10.1021/cm9016497.

(10) Aurbach, D.; Weissman, I.; Gofer, Y.; Levi, E. Nonaqueous Magnesium Electrochemistry and Its Application in Secondary Batteries. *Chem. Rec.* **2003**, *3* (1), 61–73. https://doi.org/10.1002/tcr.10051.

(11) Aurbach, D.; Lu, Z.; Schechter, A.; Gofer, Y.; Gizbar, H.; Turgeman, R.; Cohen, Y.; Moshkovich, M.; Levi, E. Prototype Systems for Rechargeable Magnesium Batteries. *Nature* **2000**, *407* (6805), 724–727. https://doi.org/10.1038/35037553.

(12) Kravchyk, K. V.; Widmer, R.; Erni, R.; Dubey, R. J. C.; Krumeich, F.; Kovalenko, M. V.; Bodnarchuk, M. I. Copper Sulfide Nanoparticles as High-Performance Cathode Materials for Mg-Ion Batteries. *Sci. Rep.* **2019**, *9* (1), 1–8. https://doi.org/10.1038/s41598-019-43639-z.

(13) Sun, X.; Bonnick, P.; Duffort, V.; Liu, M.; Rong, Z.; Persson, K. A.; Ceder, G.; Nazar, L. F. A High Capacity Thiospinel Cathode for Mg Batteries. *Energy Environ. Sci.* **2016**, *9* (7), 2273–2277. https://doi.org/10.1039/c6ee00724d.

(14) Andrews, J. L.; Mukherjee, A.; Yoo, H. D.; Parija, A.; Marley, P. M.; Fakra, S.; Prendergast, D.; Cabana, J.; Klie, R. F.; Banerjee, S. Reversible Mg-Ion Insertion in a Metastable One-Dimensional Polymorph of V_2O_5. *Chem* **2018**, *4* (3), 564–585. https://doi.org/10.1016/j.chempr.2017.12.018.

(15) Sa, N.; Wang, H.; Proffit, D. L.; Lipson, A. L.; Key, B.; Liu, M.; Feng, Z.; Fister, T. T.; Ren, Y.; Sun, C. J.; Vaughey, J. T.; Fenter, P. A.; Persson, K. A.; Burell, A.K. Is Alpha-V_2O_5 a Cathode Material for Mg Insertion Batteries? *J. Power Sources* **2016**, *323*, 44–50. https://doi.org/10.1016/j.jpowsour.2016.05.028.

(16) Spahr, M. E.; Novák, P.; Haas, O.; Nesper, R. Electrochemical Insertion of Lithium, Sodium, and Magnesium in Molybdenum(VI) Oxide. *J. Power Sources* **1995**, *54* (2), 346–351. https://doi.org/10.1016/0378-7753(94)02099-O.

(17) Hu, L.; Johnson, I. D.; Kim, S.; Nolis, G. M.; Freeland, J.; Yoo, H. D.; Fister, T. T.; McCafferty, L.; Ashton, T. E.; Darr, J. A.; Cabana, J. Tailoring the Electrochemical Activity of Magnesium Chromium Oxide Towards Mg Batteries Through Control of Size and Crystal Structure. *Nanoscale* **2019**, *11*, 639–646. https://doi.org/10.1039/C8NR08347A.

(18) McColl, K.; Johnson, I.; Corà, F. Thermodynamics and Defect Chemistry of Substitutional and Interstitial Cation Doping in Layered α-V_2O_5. *Phys. Chem. Chem. Phys.* **2018**, *20* (22), 15002–15006. https://doi.org/10.1039/c8cp02187b.

(19) Wang, R. Y.; Wessells, C. D.; Huggins, R. A.; Cui, Y. Highly Reversible Open Framework Nanoscale Electrodes for Divalent Ion Batteries. *Nano Lett.* **2013**, *13* (11), 5748–5752. https://doi.org/10.1021/nl403669a.

(20) Gu, Y.; Katsura, Y.; Yoshino, T.; Takagi, H.; Taniguchi, K. Rechargeable Magnesium-Ion Battery Based on a $TiSe_2$ Cathode with *d-p* Orbital Hybridized Electronic Structure. *Sci. Rep.* **2015**, *5* (June), 1–9. https://doi.org/10.1038/srep12486.

(21) Huang, Z. D.; Masese, T.; Orikasa, Y.; Mori, T.; Minato, T.; Tassel, C.; Kobayashi, Y.; Kageyama, H.; Uchimoto, Y. $MgFePO_4F$ as a Feasible Cathode Material for Magnesium Batteries. *J. Mater. Chem. A* **2014**, *2* (30), 11578–11582. https://doi.org/10.1039/c4ta01779j.

(22) Orikasa, Y.; Masese, T.; Koyama, Y.; Mori, T.; Hattori, M.; Yamamoto, K.; Okado, T.; Huang, Z. D.; Minato, T.; Tassel, C.; Kim, J.; Kobayashi, Y.; Abe, T.; Kageyama, H.; Uchimoto, Y. High Energy Density Rechargeable Magnesium Battery Using Earth-Abundant and Non-Toxic Elements. *Sci. Rep.* **2014**, *4*, 1–6. https://doi.org/10.1038/srep05622.

(23) Lee, B.; Jo, E.; Choi, J.; Kim, H.; Yu, S.; Kim, H.; Oh, S. H. Cr-Doped Lithium Titanate Nanocrystals as Mg Ion Insertion Materials for Mg Batteries. **2019**. https://doi.org/c9ta08362f.

(24) Bo, S. H.; Grey, C. P.; Khalifah, P. G. Defect-Tolerant Diffusion Channels for Mg^{2+} Ions in Ribbon-Type Borates: Structural Insights into Potential Battery Cathodes MgVBO4 and $Mg_xFe_{2-x}B_2O_5$. *Chem. Mater.* **2015**, *27* (13), 4630–4639. https://doi.org/10.1021/acs.chemmater.5b01040.

(25) Sun, X.; Blanc, L.; Nolis, G. M.; Bonnick, P.; Cabana, J.; Nazar, L. F. $NaV_{1.25}Ti_{0.75}O_4$: A Potential Post-Spinel Cathode Material for

Mg Batteries. *Chem. Mater.* **2018**, *30* (1), 121–128. https://doi.org/10.1021/acs.chemmater.7b03383.

(26) Sa, N.; Kinnibrugh, T. L.; Wang, H.; Sai Gautam, G.; Chapman, K. W.; Vaughey, J. T.; Key, B.; Fister, T. T.; Freeland, J. W.; Proffit, D. L.; Chupas, P. J.; Ceder, G.; Bareno, J. G.; Bloom, I. D.; Burrell, A. K. Structural Evolution of Reversible Mg Insertion into a Bilayer Structure of $V_2O_5{\cdot}nH_2O$ Xerogel Material. *Chem. Mater.* **2016**, *28* (9), 2962–2969. https://doi.org/10.1021/acs.chemmater.6b00026.

(27) Kim, C.; Phillips, P. J.; Key, B.; Yi, T.; Nordlund, D.; Yu, Y. S.; Bayliss, R. D.; Han, S. D.; He, M.; Zhang, Z.; Burrell, A. K.; Klie, R. F.; Cabana, J. Direct Observation of Reversible Magnesium Ion Intercalation into a Spinel Oxide Host. *Adv. Mater.* **2015**, *27* (22), 3377–3384. https://doi.org/10.1002/adma.201500083.

(28) Yoo, H. D.; Jokisaari, J. R.; Yu, Y. S.; Kwon, B. J.; Hu, L.; Kim, S.; Han, S. D.; Lopez, M.; Lapidus, S. H.; Nolis, G. M.; Ingram, B. J.; Bolotin, I. L.; Ahmed, S.; Klie, R. F.; Vaughey, J. T.; Fister, T. T.; Cabana, J. Intercalation of Magnesium into a Layered Vanadium Oxide with High Capacity. *ACS Energy Lett.* **2019**, *4*, 1528–1534. https://doi.org/10.1021/acsenergylett.9b00788.

(29) Kaveevivitchai, W.; Jacobson, A. J. High Capacity Rechargeable Magnesium-Ion Batteries Based on a Microporous Molybdenum-Vanadium Oxide Cathode. *Chem. Mater.* **2016**, *28*, 4593–4601. https://doi.org/10.1021/acs.chemmater.6b01245.

(30) An, Q.; Li, Y.; Deog Yoo, H.; Chen, S.; Ru, Q.; Mai, L.; Yao, Y. Graphene Decorated Vanadium Oxide Nanowire Aerogel for Long-Cycle-Life Magnesium Battery Cathodes. *Nano Energy* **2015**, *18*, 265–272. https://doi.org/10.1016/j.nanoen.2015.10.029.

(31) Verrelli, R.; Black, A. P.; Pattanathummasid, C.; Tchitchekova, D. S.; Ponrouch, A.; Oró-Solé, J.; Frontera, C.; Bardé, F.; Rozier, P.; Palacín, M. R. On the Strange Case of Divalent Ions Intercalation in V_2O_5. *J. Power Sources* **2018**, No. June, 1–11. https://doi.org/10.1016/j.jpowsour.2018.08.024.

(32) Gershinsky, G.; Yoo, H. D.; Gofer, Y.; Aurbach, D. Electrochemical and Spectroscopic Analysis of Mg^{2+} Intercalation into Thin Film Electrodes of Layered Oxides: V_2O_5 and MoO_3. *Langmuir* **2013**, *29*, 10964–10972. https://doi.org/10.1016/j.solidstatesciences.2006.09.001.

(33) Augustyn, V.; Come, J.; Lowe, M. A.; Kim, J. W.; Taberna, P.-L.; Tolbert, S. H.; Abruña, H. D.; Simon, P.; Dunn, B. High-Rate Electrochemical Energy Storage through Li^+ Intercalation Pseudocapacitance. *Nat. Mater.* **2013**, *12* (June), 518–522. https://doi.org/10.1038/nmat3601.

(34) Griffith, K. J.; Wiaderek, K. M.; Cibin, G.; Marbella, L. E.; Grey, C. P. Niobium Tungsten Oxides for High-Rate Lithium-Ion Energy Storage. *Nature* **2018**, *559* (7715), 556–563. https://doi.org/10.1038/s41586-018-0347-0.

(35) Wilkening, M.; Iwaniak, W.; Heine, J.; Epp, V.; Kleinert, A.; Behrens, M.; Nuspl, G.; Bensch, W.; Heitjans, P. Microscopic Li Self-Diffusion Parameters in the Lithiated Anode Material $Li_{4+x}Ti_5O_{12}$($0 \le x \le 3$) Measured By ^{7}Li Solid State NMR. *Phys. Chem. Chem. Phys.* **2007**, *9* (47), 6199–6202. https://doi.org/10.1039/b713311a.

(36) Griffith, K. J.; Forse, A. C.; Griffin, J. M.; Grey, C. P. High-Rate Intercalation without Nanostructuring in Metastable Nb_2O_5 Bronze Phases. *J. Am. Chem. Soc.* **2016**, *138* (28), 8888–8899. https://doi.org/10.1021/jacs.6b04345.

(37) Bashian, N. H.; Zhou, S.; Zuba, M.; Ganose, A. M.; Stiles, J. W.; Ee, A.; Ashby, D. S.; Scanlon, D. O.; Piper, L. F. J.; Dunn, B.; Melot, B. C. Correlated Polyhedral Rotations in the Absence of Polarons during Electrochemical Insertion of Lithium in ReO_3. *ACS Energy Lett.* **2018**, *3*, 2513–2519. https://doi.org/10.1021/acsenergylett.8b01179.

(38) Qian, S.; Yu, H.; Cheng, X.; Zheng, R.; Zhu, H.; Liu, T.; Shui, M.; Xie, Y.; Shu, J. Rapid and Durable Electrochemical Storage Behavior Enabled by $V_4Nb_{18}O_{55}$ Beaded Nanofibers: A Joint Theoretical and Experimental Study. *J. Mater. Chem. A* **2018**, *6*, 17389–17400. https://doi.org/10.1039/C8TA05447A.

(39) McColl, K.; Cora, F. Mg_{2+} Storage and Mobility in Anatase TiO_2: The Role of Frustrated Coordination. *J. Mater. Chem. A* **2019**, *7*, 3704–3713. https://doi.org/10.1039/c8ta09939a.

(40) Rong, Z.; Malik, R.; Canepa, P.; Gautam, G. S.; Liu, M.; Jain, A.; Persson, K.; Ceder, G. Materials Design Rules for Multivalent Ion Mobility in Intercalation Structures. *Chem. Mater.* **2015**, *27*, 6016–6021. https://doi.org/10.1021/acs.chemmater.5b02342.

(41) Börrnert, C.; Carrillo-Cabrera, W.; Simon, P.; Langbein, H. $V_{2.38}Nb_{10.7}O_{32.7}$: A V_2O_5-Nb_2O_5 Mixed Oxide Tunnel Structure Related to the Tetragonal Tungsten Bronzes. *J. Solid State Chem.* **2010**, *183* (5), 1038–1045. https://doi.org/10.1016/j.jssc.2010.02.018.

(42) Darr, J. A.; Zhang, J.; Makwana, N. M.; Weng, X. Continuous Hydrothermal Synthesis of Inorganic Nanoparticles; Applications and Future Directions. *Chem. Rev.* **2017**, *117* (17), 11125–11238. https://doi.org/10.1021/acs.chemrev.6b00417.

(43) Gruar, R.; Tighe, C.; Darr, J. Scaling-up a Confined Jet Reactor for the Continuous Hydrothermal Manufacture of Nanomaterials. *Ind. Eng. Chem. Res.* **2013**, *52* (16), 5270–5281.

(44) Dovesi, R.; Erba, A.; Orlando, R.; Zicovich-Wilson, C. M.; Civalleri, B.; Maschio, L.; Rérat, M.; Casassa, S.; Baima, J.; Salustro, S.; Kirtman, B. Quantum-Mechanical Condensed Matter Simulations with CRYSTAL. *Wiley Interdiscip. Rev. Comput. Mol. Sci.* **2018**, *8* (4), 1–36. https://doi.org/10.1002/wcms.1360.

(45) Corà, F.; Alfredsson, M.; Mallia, G.; Middlemiss, D. S.; Mackrodt, W. C.; Dovesi, R.; Orlando, R. The Performance of Hybrid Density Functionals in Solid State Chemistry. In *Principles and Applications of Density Functional Theory in Inorganic Chemistry II. Structure and Bonding, vol 113*; Springer: Berlin, Heidelburg, 2004; pp 171–232.

(46) Monkhorst, H. J.; Pack, J. D. Special Points for Brillouin-Zone Integretions. *Phys. Rev. B* **1976**, *13* (12), 5188–5192. https://doi.org/10.1103/PhysRevB.13.5188.

(47) Grimme, S.; Antony, J.; Ehrlich, S.; Krieg, H. A Consistent and Accurate Ab Initio Parametrization of Density Functional Dispersion Correction (DFT-D) for the 94 Elements H-Pu. *J. Chem. Phys.* **2010**, *132*, 154014. https://doi.org/10.1063/1.3382344.

(48) Gime, X.; Bofill, J. M.; Gonza, J. Algorithm to Evaluate Rate Constants for Polyatomic Chemical Reactions. II. Applications. *J. Comput. Chem.* **2007**, *28* (Sfb 858), 2111–2121. https://doi.org/10.1002/jcc.

(49) Grimme, S.; Hansen, A.; Brandenburg, J. G.; Bannwarth, C. Dispersion-Corrected Mean-Field Electronic Structure Methods. *Chem. Rev.* **2016**, *116* (9), 5105–5154. https://doi.org/10.1021/acs.chemrev.5b00533.

(50) de Groot, F.; Kotani, A. *Core Level Spectroscopy of Solids*; CRC Press: Department of chemistry, Utrecht University, Netherlands, 2008.

(51) Yiwata, N.; Watada, A.; Yamamuro, T.; Hayashi, Y.; Ohsawa, T.; Fujikawa, T.; Tani, K. Near Edge X-Ray Absorption Fine Structure Spectroscopy Studies of Single-Crystalline V_2O_5 Nanowire Arrays. *J. Synchrotron Radiat.* **1998**, *5* (3), 1146–1148. https://doi.org/10.1107/s0909049597018670.

(52) Abbate, M.; Pen, H.; Czyzyk, M. T.; de Groot, F. M. F.; Fuggle, J. C.; Ma, Y. J.; Chen, C. T.; Sette, F.; Fujimori, A.; Ueda, Y.; Kosuge, K. Soft X-Ray Absorption Spectroscopy of Vanadium Oxides. *J. Electron Spectros. Relat. Phenomena* **1993**, *62* (1–2), 185–195. https://doi.org/10.1016/0368-2048(93)80014-D.

(53) Brik, M. G.; Ogasawara, K.; Ikeno, H.; Tanaka, I. Fully Relativistic Calculations of the $L_{2,3}$-Edge XANES Spectra for Vanadium Oxides. *Eur. Phys. J. B* **2006**, *51* (3), 345–355. https://doi.org/10.1140/epjb/e2006-00243-5.

(54) Eyert, V.; Höck, K.-H. Electronic Structure of V_2O_5: Role of Octahedral Deformations. *Phys. Rev. B* **1998**, *57* (20), 12727–12737. https://doi.org/10.1103/PhysRevB.57.12727.

(55) Maganas, D.; Roemelt, M.; Hävecker, M.; Trunschke, A.; Knop-Gericke, A.; Schlögl, R.; Neese, F. First Principles Calculations of the Structure and v L-Edge X-Ray Absorption Spectra of V_2O_5 Using Local Pair Natural Orbital Coupled Cluster Theory and Spin-Orbit Coupled Configuration Interaction Approaches. *Phys. Chem. Chem. Phys.* **2013**, *15* (19), 7260–7276. https://doi.org/10.1039/c3cp50709b.

(56) Cartier, C.; Tranchant, A.; Verdaguer, M.; Messina, R.; Dexpert, H. X-Ray Diffraction and X-Ray Absorption Studies of the Structural Modifications Induced by Electrochemical Lithium Intercalation into V_2O_5. *Electrochim. Acta* **1990**, *35* (5), 889–898. https://doi.org/10.1016/0013-4686(90)90086-F.

(57) Soriano, L.; Abbate, M.; Fuggle, J. C.; Jiménez, M. A.; Sanz, J. M.; Mythen, C.; Padmore, H. A. The O 1*s* X-Ray Absorption Spectra of Transition-Metal Oxides: The TiO_2 -ZrO_2 -HfO_2 and V_2O_5 -Nb_2O_5 -Ta_2O_5 Series. *Solid State Commun.* **1993**, *87* (8), 699–703. https://doi.org/10.1016/0038-1098(93)90209-6.

(58) Sugiura, C.; Kitamura, M.; Muramatsu, S. Niobium L_3 and L_2 X-ray Absorption-edge Spectra of Nb_2O_5 and NH_4NbF_6. *J. Phys.* **1988**, *49* (9), 1095–1099.

(59) Cherkashenko, V. M.; Korotin, M. A.; Anisimov, V. I.; Shumilov, V. V.; Galakhov, V. R.; Kellerman, D. G.; Zubkov, V. G.; Kurmaev, E. Z. X-Ray Spectra and Electronic Structure of Li_xNbO_2 Superconductor and Other Niobium Oxide Compounds. *Zeitschrift für Phys. B Condens. Matter* **1994**, *93* (4), 417–424. https://doi.org/10.1007/BF01314244.

(60) Yoshida, H.; Tanaka, T.; Yoshida, T.; Funabiki, T.; Yoshida, S. Control of the Structure of Niobium Oxide Species on Silica by the Equilibrium Adsorption Method. *Catal. Today* **1996**, *28* (1–2), 79–89. https://doi.org/10.1016/0920-5861(95)00232-4.

(61) Ichikuni, N.; Yanagase, F.; Mitsuhara, K.; Hara, T.; Shimazu, S. Nb K- and L_3-Edges XAFS Study on the Structure of Supported Nb Carbide Catalyst. *J. Phys. Conf. Ser.* **2016**, *712* (1), 8–12. https://doi.org/10.1088/1742-6596/712/1/012060.

(62) Ling, C.; Suto, K. Thermodynamic Origin of Irreversible Magnesium Trapping in Chevrel Phase Mo_6S_8: Importance of Magnesium and Vacancy Ordering. *Chem. Mater.* **2017**, *29* (8), 3731–3739. https://doi.org/10.1021/acs.chemmater.7b00772.

(63) Hannah, D. C.; Sai Gautam, G.; Canepa, P.; Ceder, G. On the Balance of Intercalation and Conversion Reactions in Battery Cathodes. Adv. Energy Mater. 2018, 8 (20), 1–12. https://doi.org/10.1002/aenm.201800379.

FOR TABLE OF CONTENTS ONLY

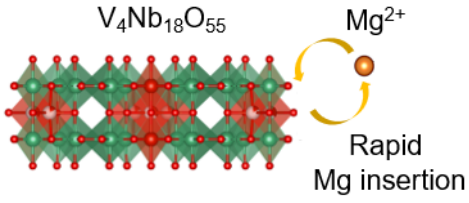

The tetragonal tungsten bronze, $V_4Nb_{18}O_{55}$, displays relatively rapid Mg^{2+} intercalation, due to rapid Mg diffusion pathways present in the structure. This family of compounds are therefore exciting candidate electrodes for next-generation rechargeable Mg batteries.